KAUNAS UNIVERSITY OF TECHNOLOGY

FACULTY OF MATHEMATICS AND NATURAL SCIENCES

Bhargesh Kandarp Shukla

DOSIMETRY IN MAGNETIC FIELDS USING IONIZATION CHAMBERS

Final Master Degree Project

Supervisor

Prof. Dr. Diana Adlienė (KTU)

KAUNAS, 2017

KAUNAS UNIVERSITY OF TECHNOLOGY

FACULTY OF MATHEMATICS AND NATURAL SCIENCES

DOSIMETRY IN MAGNETIC FIELDS USING IONIZATION CHAMBERS

Final Master's Degree Project

Medical Physics (code 621B92002)

Supervisor

(signature) Prof. Dr. Diana Adlienė

(date)

(signature) Prof. Dr. Oliver Jäkel

(date)

(Signature) Dr. Asja Pfaffenberger

(date)

Reviewer

(Signature) Doc. dr. Vardenis Pavardenis

(date)

Project prepared by

(signature) Bhargesh Kandarp Shukla

(date)

KAUNAS, 2017

KAUNAS UNIVERSITY OF TECHNOLOGY

Faculty of Mathematics and Natural Sciences

(Faculty)

Bhargesh Kandarp Shukla

(Student's name, surname)

Medical Physics (code 621B92002)

(Title and code of study programme)

"DOSIMETRY IN MAGNETIC FIELDS USING IONIZATION CHAMBERS"

DECLARATION OF ACADEMIC INTEGRITY

___ _____ ____

Kaunas

I confirm that the final project of mine, **Bhargesh Kandarp Shukla**, on the subject *DOSIMETRY IN MAGNETIC FIELDS USING IONIZATION CHAMBERS* is written completely by myself; all the provided data and research results are correct and have been obtained honestly. None of the parts of this thesis have been plagiarized from any printed, internet-based or otherwise recorded sources. All direct and indirect quotations from external resources are indicated in the list of references. No monetary funds (unless required by law) have been paid to anyone for any contribution to this thesis.

I fully and completely understand that any discovery of any manifestations/case/facts of dishonesty inevitably results in me incurring a penalty according to the procedure(s) effective at Kaunas University of Technology.

_____ _____

(name and surname filled in by hand) (signature)

Shukla, Bhargesh Kandarp. Dosimetry in Magnetic Fields Using Ionization Chambers. Master‘s thesis in Medical physics / supervisors prof. Diana Adlienė (KTU) and prof. Dr. Oliver Jäkel (German Cancer Research Center); the Faculty of Mathematics and Natural Sciences, Kaunas University of Technology.
Research area and field: Biomedical Sciences, Medicine and Health
Key words: Dosimetry, Ionization chamber, MRgRT, Monte-Carlo simulation, EGSnrc code.
Kaunas, 2017. 78 p.

SUMMARY

Adaptive treatment planning using a device that integrates magnetic resonance imaging (MRI) and a radiation therapy unit is the key development in radiation oncology to further improve targeted dose delivery and avoid complications, since MRI provides excellent soft-tissue visualization. The designs of these modalities aim to produce simultaneous and unimpeded operation of an MRI and a medical linear accelerator. However, the presence of a magnetic field influences the response of radiation detectors due to the Lorentz force acting on the secondary electrons. The objective of this project was to determine the response of three recently developed MR-compatible ionization chambers in magnetic fields of different field strengths and field orientations. The response of the MR-compatible Exradin ionization chambers was investigated both by means of experiments and simulations. For the magnetic field perpendicular to photon beam and ion chamber axis, both experiments and simulations could be conducted, and the experimental measurements showed good agreement with the simulation results. In this orientation, the measured chamber response showed a significant increase with magnetic flux density. Simulations only were carried out for the other two orientations: the magnetic field parallel to the chamber axis as well as parallel to the beam. There was very little change in chamber response for all magnetic flux densities in both orientations. Overall, the chamber response in a magnetic field could be modelled well using EGSnrc Monte-Carlo simulations within measurement accuracy.

Shukla, Bhargesh Kandarp. Dozimetrija magnetiniuose laukuose naudojant jonizacines kameras. Magistro baigiamasis projektas / vadovas prof. dr. Diana Adlienė (KTU) ir prof. Dr. Oliver Jäkel (German Cancer Research Center); Kauno technologijos universitetas, Matematikos ir gamtos mokslų fakultetas.
Mokslo kryptis ir sritis: biomedicinos mokslai, medicina ir sveikata.

Reikšminiai žodžiai: dozimetrija, jonizacine kamera, MRgRT, Monte-Karlo modeliavimas, EGSnrc kodas.

Kaunas, 2017. 78 p.

SANTRAUKA

Gydymo planavimas integruojant magnetinio rezonanso vaizdinimą (MRI) į spindulinės terapijos įrenginį yra svarbus žingsnis spindulinėje terapijoje, siekiant pagerinti į taikinį (auglį) suvedamos dozės tikslumą ir išvengti kompolikacijų, nes MRI pasižymi puikia minkštųjų audinių vizualizacija. Kuriant tokią įrangą, siekiama, kad magnetinio rezonanso vaizdinimo įrenginys ir medicininis greitintuvas funcijonuotų vienu metu netrukdydami vienas kitam atlikti priskirtų funkcijų. Tačiau magnetinis laukas daro įtaką detektoriais registruojamam signalui, nes pasireiškia antrinius elektronus veikianti Lorenco jėga. Šio projekto tikslas buvo nustatyti magnetinio lauko (integruotas MRI įrenginys) poveikį signalams, registruojamiems naudojant tris skirtingas naujai sukurtas jonizacines kameras, atsižvelgiant į magnetinio lauko stiprumą ir orientaciją kamerų atžvilgiu. Suderintų su MRI Exradin tipo jonizacinių kamerų registravimo efektyvumas buvo tiriamas tiek eksperimentiškai, tiek matematinio modeliavimo būdu. Atvejis, kai magnetinis laukas yra statmenas fotonų srautui ir jonizacinės kameros ašiai buvo tiriamas abiem minėtais metodais. Eksperimentiniai rezultatai gerai sutapo su modeliavimo rezultais, ir buvo nustatyta, kad jonizacinės kameros jautrumas didėjo, didėjant magnetinio lauko stiprumui. Kitiems dviems atvejams tirti - kai magnetinis laukas orientuotas lygiagrečiai jonizacinės kameros ašiai ir kai laukas orirntuotas lygiagrečiai fotonų spinduliui,- buvo pritaikytas tik matematinis modeliavimas. Esant tokioms magnetinio lauko orientacijoms, buvo stebimas tik labai nedidelis jautrio pokytis, kintant magnetinio lauko stiprumui. Darbe parodyta, kad magnetinio lauko įtaka jonizacine kamera registruojamam signalui gali būti sėkmingai nustatoma atliekant Monte Karlo modeliavimą naudojant EGSnrc programinį paketą, pateikiant modeliavimo rezultatą tokiu pat tikslumu, kaip ir matavimo rezultatas.

Table of Contents

List of Figures

List of Tables

List of Abbreviations

CT	Computed Tomography
CTV	Clinical Target Volume
EBRT	External Beam Radiation Therapy
EGS	Electron Gamma Shower
IAEA	International Atomic Energy Agency
ICRU	International Commission on Radiation Units and Measurements
IG(A)RT	Image Guided (Adaptive) Radiation Therapy
ITV	Internal Target Volume
Linac	Linear accelerator
MC	Monte-Carlo
MRgRT	Magnetic Resonance guided Radiation Therapy
MRI	Magnetic Resonance Imaging
OARs	Organ At Risk
PET	Positron Emission Tomography
PTV	Planning Target Volume
RR	Range Rejection
SPECT	Single Photon Emission Computer Tomography
VRT	Variation Reduction Technique
XCSE	Photon Cross-Section Enhancement

1. Introduction

Imaging modalities in radiotherapy are necessary to delineate the tumor precisely and spare surrounding healthy tissues. Moreover, it is desirable to carry out adaptive treatment (Yan, et al., 1997). Most common methods are x-ray based (computed tomography, CT) to locate the tumor but there are drawbacks with CT in comparison to the non-invasive imaging technology like magnetic imaging resonance imaging (MRI). First, the CT images give detailed scans of inside areas of the body with poor contrast for delineation of the tumor which is mostly located in the soft tissues. MRI stands out when it comes to soft tissue visualization. Second, ionizing radiation is involved with CT scanning since it uses x-rays and exposes the patient to additional, even though small, radiation dose, while the MRI uses radiofrequency waves for imaging. Third, to implement real-time radiation therapy, MRIdian ViewRay is the first system to implement it (Dempsey, et al., 2006).

Many companies and institutes are building hybrid MRI radiotherapy devices with different orientations. The Linac-MR by Alberta Health Services (Canada) (Fallone BG, 2009) uses the magnetic field parallel to the photon beam (rotate magnet and gantry), the MR-Linac Philips-Elekta (Lagendijk, et al., 2008) uses a magnetic field perpendicular to the photon beam, the Australian MRI-Linac (Keall, et al., 2014) has an inline configuration where the photon beam is aligned parallel to the B_0 magnetic field (rotate patient) and the ViewRay MRIdian (Dempsey, et al., 2006) has the photon beam perpendicular to the magnetic field (gantry rotation).

Ionization chambers are most commonly used in radiotherapy for the characterization of the radiation beam, e.g. for the measurement of dose profiles, point dose measurement and quality assurance. The use of ionization chambers in the field of the MRI is being investigated, and the response of the chambers is known to depend on the chamber type, the magnetic flux density and the orientation between chamber axis, beam and magnetic field (M. Reynolds, 2013)(Meijsing, 2009).

In a magnetic field, secondary electrons are affected by the Lorentz force. They have been described to follow curved paths in air cavities (Raaijmakers AJ, 2007) as they also exist in ionization chambers. In a 1.5 T magnetic field, it has been shown that at tissue-air interfaces, the electrons from the tissue undergo an 180^o turn when being force back onto a semicircle in the air before they re-enter the tissue. There, they deposit their energy. The consequent dose increase seen at the interface has been termed the electron return effect (ERE) (Raaijmakers AJ, 2005).

The aim of this project is to determine the response in a magnetic field for ionization chambers with different cavity sizes. Experimental measurements and Monte-Carlo radiation transport simulations were performed using three recently developed MR-compatible ionization chambers,

namely, A19MR Farmer-type ionization chamber, A1SLMR slimline miniature ionization chamber, and A26MR micro ionization chamber (Standard Imaging Inc., 2016). The experiment was carried out using a 6 MV photon beam from a medical linear accelerator (linac, Artíste, Siemens Medical Solutions Inc., PA, USA) which was simulated using a published 6 MV spectrum (Mohan, et al., 1985). Measurement and simulation conditions were 10 cm water equivalent depth (according to international protocol, IAEA TRS-398) (IAEA, 2000) and magnetic fields that ranged from 0 to 1.1 T. The experiment was simulated using the EGSnrc (Kawrakow &Rogers, 2000) Monte-Carlo radiation transport simulation code egs_chamber (J. Wulff, 2008) including a macro for the particle transport in a magnetic field (Kawrakow & Rogers, 2000).

In this project, dose measurements in water are performed using the three ionization chambers and they are analyzed as a function of the magnetic flux density and its orientation relative to the photon beam. The experimental measurement at the German Cancer Research Centre (DKFZ), Heidelberg (Germany) was practically possible only for the magnetic field aligned perpendicular to the chamber and the beam axis. Simulations were performed with the magnetic field in all possible orientations: the magnetic field aligned perpendicular to the chamber and beam axis, the magnetic field parallel to the chamber as well as parallel to the beam axis.

Project objective and task:

The main objective of the thesis is to determine the dose response of MR-compatible ionization chambers in a magnetic field as it is present in hybrid devices which integrate MRI and radiation therapy units (Raaymakers BW, 2004). As investigated by (Meijsing, 2009) the actual dose response depends on the magnetic flux density as well as on the orientation between chamber axis, beam and magnetic field. For three selected chambers, which have not been characterized in detail with respect to their application in MRgRT before, measurements and simulations were carried out with magnetic flux densities ranging from 0 T to 1.1 T with different orientations. The chambers used were the Exradin A19MR ion chamber, Farmer-type chamber, Exradin A26MR ion chamber, Micro chamber, Exradin A1SLMR ion chamber, and Slimline mini chamber.

The objective of the thesis will be achieved through the following tasks:

1. Setup of an experimental measurement according to the current IAEA TRS-398 dosimetry protocol (IAEA, 2000), with a 6 MV beam perpendicular to the chamber and magnetic field axis.
2. Implementation of the setup in the Monte-Carlo simulation code EGSnrc by modelling all three ionization chambers.
3. Carrying out simulations with the magnetic field in all relevant orientations for MRgRT: the magnetic field aligned parallel to the chamber and perpendicular to the beam axis, the

magnetic field aligned perpendicular to both the chamber and the beam axis as well as the magnetic field aligned parallel to the beam axis and perpendicular to the chamber.

4. Comparison of measurements and simulations, analyzing of the dose response in a magnetic field for ionization chambers with different cavity sizes.

2. Literature Review

This section explains the fundamental knowledge related to this thesis. Describing about radiation with matter and the general principle of the dosimetry in presence of a magnetic field. Further, Monte-Carlo radiation transport simulations for calculating the dose in three dimensional volumes are described. The potential of MR-guided radiation therapy is discussed as well as designs for integrated MRgRT devices presented, followed by a review on prior work on dosimetry in magnetic fields and finally, the objective and task of this project are defined.

2.1 History and basics of external beam radiation therapy (EBRT)

2.1.1 Brief history of EBRT

In external beam radiation therapy treatment, high energy collimated x-ray beams are used with the aim to reach and sterilize tumors while avoiding high doses in normal tissues.

Treatment of cancer using external beams looks back on 120 years of history and started a few months after the discovery of x-rays by the German/Dutch scientist Wilhelm Röntgen in 1895 (Science, 1957). **Figure 1** shows for prostate how the development from kilovoltage x-rays to cobalt devices and medical linear accelerators (linacs), a refinement in technology, and the use of particle therapy can potentially increase the dose to the tumour at the same level of normal tissue toxicity.

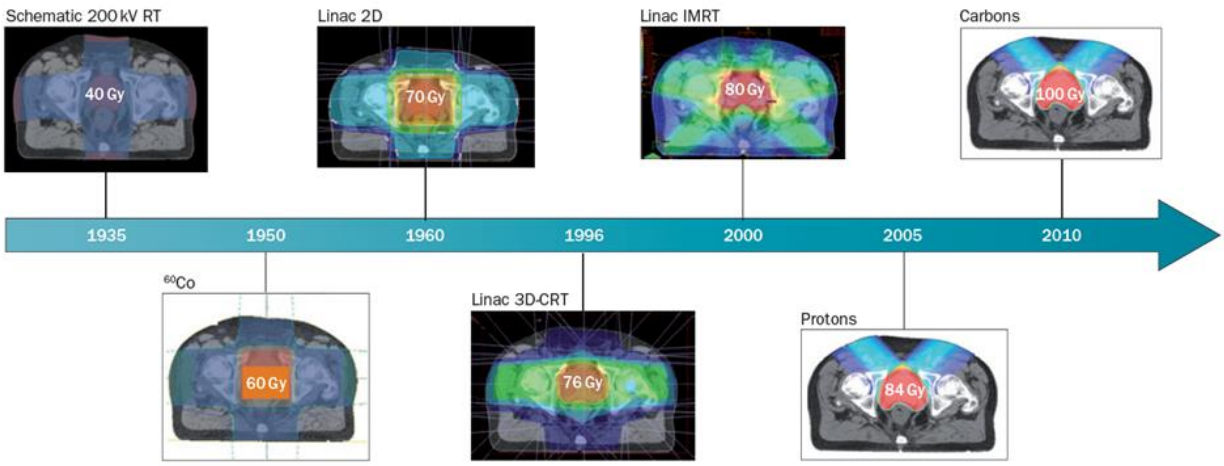

Figure 1. The potential increase of dose to the target volume at the same level of normal tissue toxicity. Reproduced from (Thariat, 2013). Prostate cancer radiotherapy 1935-2010. Prostate cancer irradiation is a good example for the improvement of radiotherapy.

2.1.2 Radiation interaction with matter

The detection, characterization and impact of radiation are completely dependent upon their interaction with matter. Indirectly ionizing radiation (here gamma rays and x-rays) are radiation particles or photons with no charge, but during interaction with matter they can transfer energy to charged particles, atom electrons due to electromagnetic interactions (Sprawls, n.d.).

The interaction of photons with matter include several different processes, each process is strongly dependent on the energy of photons and upon the density and atomic number of the absorbing medium. Some of the important processes involved are:

Rayleigh effect:

At a point when a photon interacts with an atom, it may possibly impart some energy to the atom. The photon may get deflected with no energy transfer, this process is called Rayleigh scattering and is most likely for low energy photons.

Photoelectric effect:

The most probable destiny of a photon having a slightly higher energy than its atomic electrons' binding energy is photoelectric absorption. Here, the photon transfers all the energy to the electrons and ends its own existence. The electron will get away from its orbit with a kinetic energy equivalent to the difference between the initial photon energy and its own binding energy. Similarly, as with ionization delivered by any process, secondary radiation is started, here, by the photoelectron which has the adequate energy to deliver additional ionization and excitation of orbital electrons. Likewise, filling of the electron vacancy left behind by the photoelectron results in characteristics x-rays. The kinetic energy of photoelectron ejected (E_e) is equal to incoming photon energy (hv) subtract the binding energy of the photoelectron in its original shell (E_b):

$$E_e = hv \times E_b \tag{1}$$

The probability of photoelectric absorption per unit mass is approximately proportional to:

$$T_{(photoelectric)} = Constant \times \frac{Z^N}{E^{3.5}} \tag{2}$$

Here, Z is the atomic number, and exponent n varies between 4 and 5, E is incident photon energy.

Compton Effect:

This is the most dominant type of interaction for medium energy photons (0.3 to 10 MeV). In this process, a photon with sufficient energy interacts with an atomic electron and pushes it out of the orbit, while retaining a portion of its energy and continuing to move on another path. Thus, Compton Effect involves absorption and scattering. The amount of energy lost by the photon determines the angle for the scattered photon with respect to the original direction of travel. The

scattered photon with low energy interacts again and may undergo photoelectric or Rayleigh effects. The free electron produced with quite high energy may act like a beta particle and produce further secondary ionization and excitation before coming to rest. The shift of the wavelength increased with scattering angle in relation to Compton formula:

$$\lambda_f - \lambda_i = \Delta\lambda = \frac{h}{m_e c}(1 - \cos\theta) \quad (3)$$

Pair production:

This process takes place for photon energies above 1.022 MeV, where photons may be converted into electron and positron each having a rest mass of 0.511 MeV, under the influence of the electromagnetic field of a nucleus. A positronium is formed, when a positron propagates few millimeters unless it couples with an electron. Later it annihilates and two photons of energy 0.511 MeV are emitted with an angle of approximately 180^o between each other.

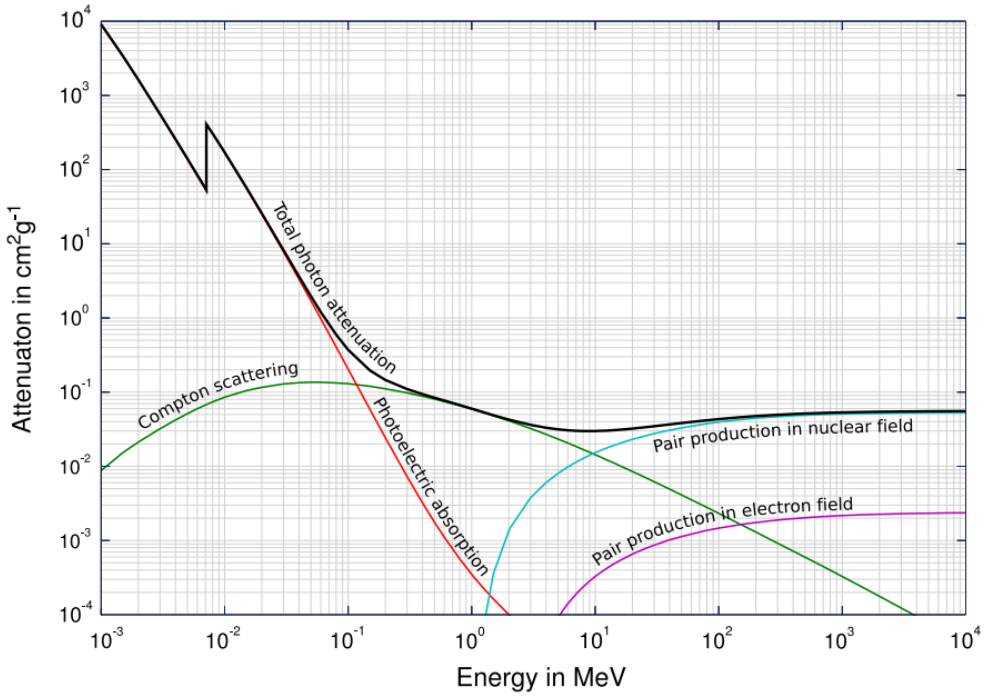

Figure 2. Mass Attenuation of water according to photon energy for different modes of interaction (Wikimedia Commans, 2017)

In **Figure 2**, the total mass absorption coefficient in water is shown as the sum of the absorption coefficients for photo effect, Compton scattering and pair production. For soft tissue and photon energies above around 30 keV, the Compton effect gets dominant; i.e. more photons are scattered. **Figure 3** shows the regions in which each type of photon interaction dominates as a function of photon energy and atomic number of the absorber.

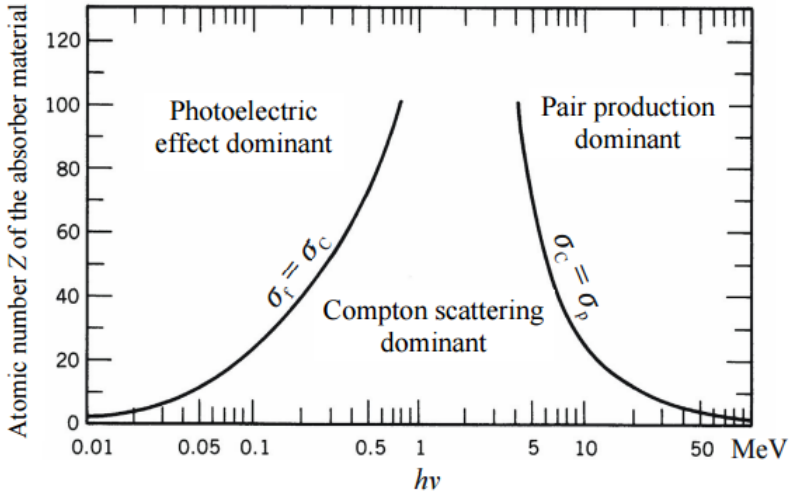

Figure 3. Dominating effects in the x-ray interaction, according to the atom and energy number. Reproduced from (Bille & Schlegel, 2002)

The absorbed radiation dose is directly correlated with the energy of the beam, where an accurate absorbed dose measurement is critical. The photons entering the tissue create secondary electrons, which deposit the dose nearby in the medium. Different materials and densities at the air-tissue interface result in a build-up of the depth dose curve as shown in **Figure 4**. The photon depth dose curve is used to determine the amount of monitor units that a treatment machine requires to deliver a particular dose to a particular depth. With larger penetration depth, more photons are absorbed and eventually less dose is deposited (Schlegel & Bille, 2002).

Low energy photons are not used in treatment as they do not reach deep-seated tumors with adequate dose. Linacs with 6 MV energy photons deposit more dose in deeper regions, and thus avoid the building up of higher doses on the surface (Schlegel & Bille, 2002).

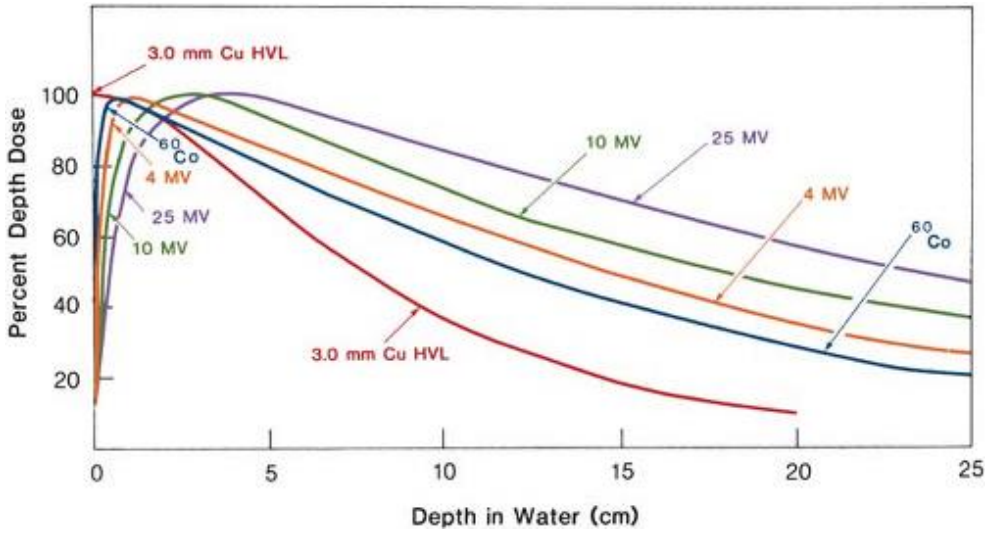

Figure 4. The depth dose curve for photons with different energies. Reproduced from (drzezo, 2016).

2.1.3 Biological effects of radiation

The energy absorbed is low but the biological effects to the body are serious, which is one of the characteristics of ionization radiation on living cells. High energy photon radiation can damage genes (DNA) and some of the molecules of the cell. These ionizing radiation are dangerous, as atoms in living cells become ionized and it leads to one of the following three things: cell death, cell repairs itself or cell mutates incorrectly and can become cancerous. All cells are affected in different ways.

The goal of the radiation therapy is to cure or shrink early stage cancer, stop cancer from recurring in another area. The treatment is delivered in regular intervals called fractionation, which allows normal tissues to repair of radiation damage, while tumor tissue, generally less efficient at repair, does not recover (Baskar, et al., 2014).

2.1.4 Image Guided (Adaptive) Radiation Therapy (IG(A)RT)

Major technological innovations have resulted in advanced radiation therapy planning, delivery and verification. The use of CT imaging for target volume contour paired with the availability of computer-controlled treatment planning and delivery systems have led to a conformation of radiation dose to the target tissues while sparing the nearby healthy tissues. The management of geometric uncertainties in modern radiotherapy practice conducting in the pattern of image-guided radiation therapy (IGRT) is vastly improved by the integration of various imaging modalities within the treatment room for guiding radiation delivery. (Gupta & Narayan, 2012)

IGRT should be considered necessary and natural development to a high-precision radiotherapy. From the types of radiation beam and techniques of treatment delivery, IGRT plays a vital role in reducing geometrical uncertainties related with the tumor shape and position. Besides accurate information on patient and tumor position on a quantitative scale, IGRT also gives the opportunity to verify consistency between the planned and the actual treatment geometry that involves adaptation to daily varying results, in order to improve the dose delivery. The resource-intensive nature of dose delivery and increasing dose from additional imaging are the two main concerns with IGRT. MRI guided radiotherapy therapy can overcome the above mentioned concerns**.** The need of imaging with respect to radiation treatment can be divided into four parts:

Treatment volume definition and characterization

The goal of imaging for treatment volume definition and characterization is to delineate the tumor in high contrast to its surroundings in 3D with high spatial resolution. Currently, a few sorts of imaging modalities are accessible in the pre-treatment phase. Examples of such modalities are CT, positron emission tomography (PET), single photon emission tomography (SPECT), ultrasound

and magnetic resonance imaging (MRI). Moreover, for tumor positioning these imaging modalities may help to visualize tumor tissue characteristics.

Setup rectification

Online imaging of the patient in the treatment position can be utilized to confirm the patient's setup and wherever needed, rectify everyday variations to ensure a more precise dose delivery. The resulting increment in accuracy leads to a reduction of the PTV and it diminishes the dose to healthy tissues permitting an increase of dose to the tumor volume.

Treatment plan adaptation

Currently, the patient position is adjusted to simulate the planned situation in the most practical cases. For a few circumstances the patient anatomy in the vicinity of the tumor can change significantly over a longer period of time, which may be due to the patient weight loss or tumor shrinkage. So, the new CT scan is made, and again a new treatment plan is generated.

Intra-fraction motion compensation

The motion inside the body can hamper radiation treatment, as it causes the target to make semi-periodic movement; such as kidney, pancreas, stomach, liver and the lungs. (Kitamura K, 2003), (Van Sornsen de Koste JR, 2006). A margin to the CTV, i.e. the volume of suspected tumor cell spread, is considered for this motion, creating the internal target volume (ITV) (ICRU report 50, 1993) (ICRU report 62, 1999).

From the principle of radiation therapy and its workflow, we need a good soft tissue contrast image without exposing the patient to additional harmful radiation. Moreover, the fast imaging technique with real-time monitoring and treatment would be the future aspect.

For all these reasons, MRI can be an excellent and safe modality to integrate with radiation therapy (Wolthaus JWH, 2008).

2.2 Dosimetry

Reference dosimetry and relative dosimetry are the two categories, which dosimetry at a clinical radiotherapy department is generally divided into. Reference dosimetry characterizes the 'absolute' amount of dose at a specific point of interest and relative dosimetry refers to dose measurements compared to the dose at a reference point.

2.2.1 Reference dosimetry

The reference conditions according to the international protocol IAEA TRS-398 (IAEA, 2000) for the determination of the absorbed dose to water in 6 MV photon beam and Cobalt-60 beams

include a radiation field size of 10 cm x 10 cm at isocenter. The reference point of the ionization chamber should be positioned at the depth of 10 cm for 6 MV photon beams and at 5 cm for cobalt-60. Reference dosimetry is mostly performed using an air-filled ionization chamber that measures the amount of ionizations in the measurement volume by detecting the charged particles that are produced during the ionizations. To detect these charged particles, an ionization chamber has two electrodes with a voltage difference between them which is connected to the electrometer.
The dose (Gy) from the ionization (Coulomb) can be derived (IAEA, 2000) as follows:

$$D = M_Q . N_{D,w} . k_{T,p} . k_p . k_s . k_Q \quad (4)$$

Here, M_Q is the measured charge, $N_{D,w}$ is the specific calibration factor, $k_{T,p}$ is the temperature and pressure correction factor, $k_p$is the correction for polarity effect, k_s is the correction for recombination effect andk_Q is the beam quality factor.
The calibration factor $N_{D,w}$ is provided by the calibration laboratory for each ionization chamber, so charge measured with ionization chambers can be converted into units of dose (Gy).

2.2.2 Relative dosimetry

The aim of relative dosimetry is to measure the amount of dose in one or several positions but normalized to the dose at a reference point. Relative dosimetry can be carried out using a wide variety of methods or orientations using a wide variety of detectors. Dose can, for instance, be measured inside a scanning water phantom using a detector in many positions (O'Neill MJ, 1988). In such cases, the dose distribution must be stable for the time-period of measurement. In other cases, many detectors are used at once, in any formation or pattern over the surface of a panel, and the results of those detectors can be analyzed with respect to a single reference point.
Relative dosimetry is crucial for checking and calibrating beam parameters.

2.2.3 Dosimetry with ionization chambers

In radiotherapy, dosimetry is commonly carried out by means of ionization chambers. The dose at a certain point of interest in an ionization chamber is measured, which is the measurement volume. In this thesis, the chambers used are MR-compatible (definition of “MR-compatible” Shellock, 2010). In these chambers, the C552 (air-equivalent material) electrode is mounted in the middle. The measurement volume is filled with air, so that the pressure in the chamber is the same as the surrounding air pressure. The surface of the chamber is covered with C552 and represents the electrode. The incoming ionizing radiation produces an ion electron pair in the measurement volume. A potential between the two electrodes leads to the separation of ion pairs, the ion and

electron. The electron moves towards the anode, and the amount of electrons are measured as charge (Coulomb). The created charge is proportional to the dose deposited, where the charge can be recalculated in units of dose with the calibration factor.

To determine the absorbed dose delivered to the patient (to within a few percent), an ion chamber is placed in the medium. The ionization chamber can measure the energy absorbed in the surrounding medium **Figure 5**. According to the reference dosimetry IAEA TRS-398 (IAEA, 2000), the ionization chamber is placed in a water phantom to measure dose to water.

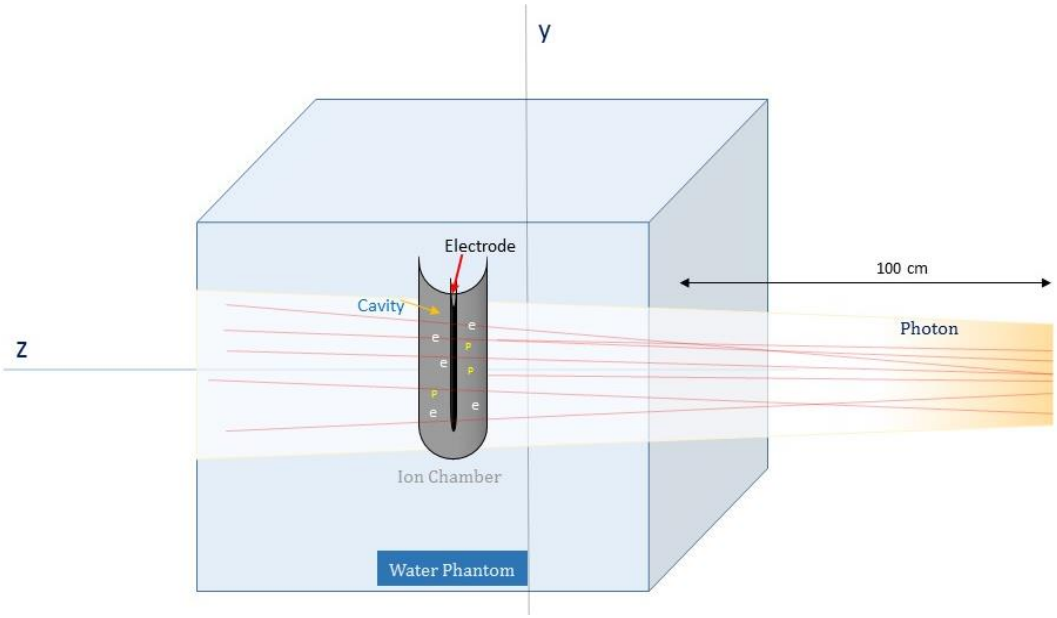

Figure 5. Extended schematic drawing of the ionization chamber's measurement volume with process of ion production from incident radiation.

2.3 Monte-Carlo radiation transport simulations

2.3.1 Review of the Monte-Carlo method for radiation transport simulation

The Monte-Carlo methods and techniques are most important and common practice in science today. The use of Monte-Carlo simulations has been around since the 1950's and in 2013 more than 104 MC works have been published, and 103 of these were set in the field of medicine or medical physics (Verhaegen, 2013). The Monte-Carlo method is mostly used for simulations of stochastic process, e.g. the interaction of radiation with matter. There are many types of implementations of Monte-Carlo methods, although the common principle remains the same.

First of all, a field of possible events is defined. Subsequently, random inputs are generated from a probability distribution over the field and the process evolution is computed for each input. Lastly, the results are totaled and the mean value and statistical precision of the quantity of interest are presented.

The random process of inputs is also referred to as histories. And the number of histories used in simulation has a direct effect on the accuracy of the simulation process as well as the time required to calculate it. The available amount of processing power and the needed accuracy should be taken into account, to determine a suitable number of histories to simulate a given scenario.

2.3.2 The EGSnrc Monte-Carlo code

The EGSnrc stands for Electron-Gamma-Shower, Monte-Carlo developed at the National Research Council (NRC) in Ottawa. It is a dedicated simulation tool for photon and electron (also positron) processes that occur in medium over the energy range of a few keV to several GeV. EGSnrc is written in MORTRAN, a structured macro based language; it provides the user with a tool to carry out particle transport and energy deposition in circumstances where experimental measurements may be impractical or expensive or may be impossible. EGSnrc depends on random number generation to generate unique particle histories on an event by event basis. To be more specific, interaction cross sections are sampled to carry out particle kinematics concordant with physical understanding. Individual events are of practical interest besides the collective effect of several events that produce an energy distribution which mimics nature and can be reproduced with defined uncertainty. Monte-Carlo simulations can be performed with a wide variety of materials as well as geometric situations. The large computational time to achieve low statistical uncertainties is the drawback of Monte-Carlo simulations, but it can be overcome with computers becoming increasingly cost effective and increasing computational speeds.

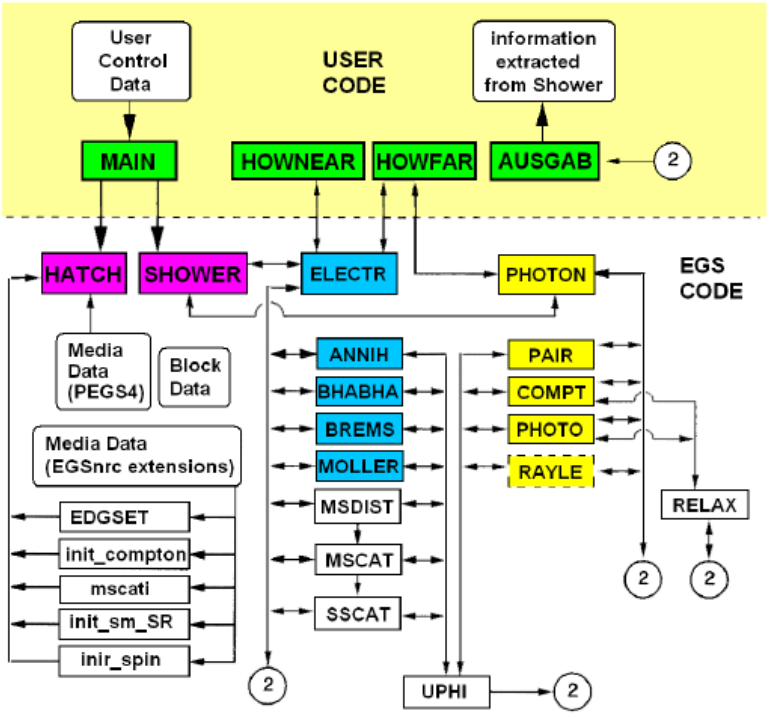

Figure 6. EGSnrc Monte-Carlo flowchart. Taken from the EGSnrc User Manual. (Rogers, et al., 2007).

The EGS code is divided into two main parts as shown in **Figure 6** (a) the user code; here, the user specific parameters are set, for example: the geometry and the output variables. (b) The EGS code: here, the simulation of the general physical processes are handled.

2.3.3 The egs_chamber user code

The egs_chamber user code is a recent addition to the EGSnrc family of user codes, developed by (J. Wulff, 2008). It is a modified version of original EGSnrc code 'cavity'. To achieve an improved efficiency with respect to the calculation of perturbation factors and ion chamber dose at more than one position inside a phantom (Kawrakow, 2006), a number of variance reduction techniques are introduced in egs_chamber.

2.3.4 Variance reduction techniques

In order to improve the efficiency of the simulations, one or more variation reduction techniques (VRT) are employed. The uncertainty of a Monte-Carlo simulation depends on the variance of the estimated quantity, calculated by:

$$\sigma(X) = \sqrt{\frac{Var(X)}{N}} \tag{5}$$

Here, N determines the number of simulated histories and Var(X) the variance of the estimated quantity. Moreover, the efficiency ϵ of a Monte-Carlo simulation can be calculated by

$$\epsilon = \frac{1}{T\,.\,\sigma^2} \tag{6}$$

Here, T is the CPU time needed to calculate a quantity of interest to a limit of estimated statistical uncertainty σ(Wulff, et al., 2008). It makes sense that $\sigma(X)$ can be improved by either increasing the number of histories calculated or decreasing the variance of estimated quantity. Any approach that leads to increase in ϵ without bringing up systematic errors can be considered a VRT (Wulff, et al., 2008).

Range Rejection (RR)

The primary idea behind range rejection is that any charged particle with shorter range than the distance to the scoring volume is rejected. A threshold is defined by the user in order to control this approximation.

Photon Cross-Section Enhancement (XCSE)

The main reason for the implementation of XCSE is that the interaction density of the photons in the cavity medium is low. The result of XCSE VRT is alike to that of photon splitting, which works by dividing a photon into N sub-photons with unvarying distribution of interaction sites

along the initial direction. The shower of particles in a region surrounding the scoring volume is amplified, and there are rules to be followed to reassure an unbiased result and equal particle weighting. For the same reason, particle splitting and Russian roulette are played in a way that each particle type has a unique statistical weight given by the XCSE factor. All these VRT are used in the thesis, in order to be considered optimal by recent standards Monte-Carlo simulations.

Russian roulette

A Russian roulette game is played with electrons that cannot reach the cavity. The electrons which are trapped in the cavity region with their energy less than the total energy (specified using E_{save} in input file) are immediately discarded, depositing their energy locally. This technique extract expected values while avoiding the events that spend much time tracking the particles having small weightage or that are unproductive.

2.3.5 Photon transport and interaction

The processes simulated in the EGSnrc code are: (a) The photoelectric effect, (b) Compton scattering, (c) Rayleigh (incoherent) scattering, and (4) Pair production. The probability of these interactions occurring is linked to their individual interaction cross sections designated$\Sigma_{Photoelectric}$,$\Sigma_{Compton}$, $\Sigma_{Rayleigh}$ and Σ_{Pair} with total probability of a photon interaction being the sum of all:

$$\Sigma_{Total} = \Sigma_{Photoelectric}+\Sigma_{Compton}+\Sigma_{Rayleigh}+\Sigma_{Pair} \quad (7)$$

EGSnrc transports a photon in the following pattern, using the above information. First, from the relation equation (8), the distance from the current particle position to an interaction site is sampled.

$$s = \frac{-lnr_1}{\Sigma_{Total}} \quad (8)$$

Here, s is the length of the path and r_1 is a random number in between 0 and 1. If the particle trajectory extends a geometric limit prior to the event (bound by HOWFAR), it is simply transported out of the current region and the whole process is repeated. Else, the particle is transported to the point of interaction. Erstwhile at the location, the type of interaction is chosen based on a second number, r_2 and the rules below:

- Rayleigh Event if $r_2<\Sigma_{Rayleigh}/\Sigma_{Total}$ (only if Rayleigh interactions are requested)
- Pair Production Event if $r_2<\Sigma_{Pair}/\Sigma_{Total}$ and $\Sigma_{\gamma}> 2m_e$
- Compton Event if $r_2< (\Sigma_{Pair}+\Sigma_{Compton})/\Sigma_{Total}$
- Photoelectric Event otherwise

Next, the differential cross section distributions are used to employ concordant kinematical information to all particles that are produce from the interaction. New particles are transported in a similar fashion until they lose all their energy or leave the applicable geometry. A single particle history is accomplished when the transport of the first particle and all its secondary particles is finished.

2.4 MR guided Radiation Therapy (MRgRT)

2.4.1 Potential of MRgRT

MRI provides better soft tissue contrast and good delineation of both tumorous tissue and organs at risk (OARs), compared to CT or any other imaging modalities. Magnetic resonance (MR) sequences have numerous parameters that can be adjusted to obtain contrasts to be related to tissue characteristics; say cell density, tissue oxygenation and tissue perfusion. Volumetric 1D, 2D, 3D data sets can be obtained in random orientation using MRI. Also, it does not use ionizing radiation and hence can be scanned multiple times without risk of increasing the patient's radiation dose. With excellent soft tissue contrast, MRI adds the possibility of actual positioning and enabling motion tracking for radiation therapy. Unique positioning of the patient and dose reconstruction is provided in real time treatment; and hence the dose certainty in the treatment process (Lagendijk, et al., 2014).

In 2009, an idea was put forward for radiotherapy with MRI scanner next door, a 1.5 T MRI installed near to the linac. Patients were transported on a trolley especially adjustable such that it can be moved between the treatment couch and the imaging device forth and back (Karlsson M, 2009). Later the IMRIS Inc. (Jaffray DA, 2014) system with a more sophisticated solution was put forward. Here, the MRI is mounted on a rail that moves in and out of the treatment room. Although it is an attractive concept, it fails to provide feedback during the radiation delivery. Further, for online image guidance during radiotherapy, integration of a linac with an MRI was proposed by (Raaymakers BW, 2004).

2.4.2 Designs of MRgRT devices

There are several designs to integrate a radiotherapy modality with an MR imaging modality. The first design was proposed by the UMC Utrecht in collaboration with ELEKTA (ELEKTA AB, Stockholm, Sweden) and Philips (Philips Medical Systems, Best, The Netherlands). **Figure 7**, shows the 6 MV linac combined with a 1.5 T MR scanner (Stark R, 2011). The MR scanner is made in such a way to allow the beam to pass through to the isocenter of the MR scanner with a

maximum field size of 24 cm in the head-feet direction. The 1.5 T MR scanner provides a similar image quality to a diagnostic MRI device. The new design of the Utrecht MR-Linac integrating 8 MV linac with 1.5 T MRI scanner was installed recently.

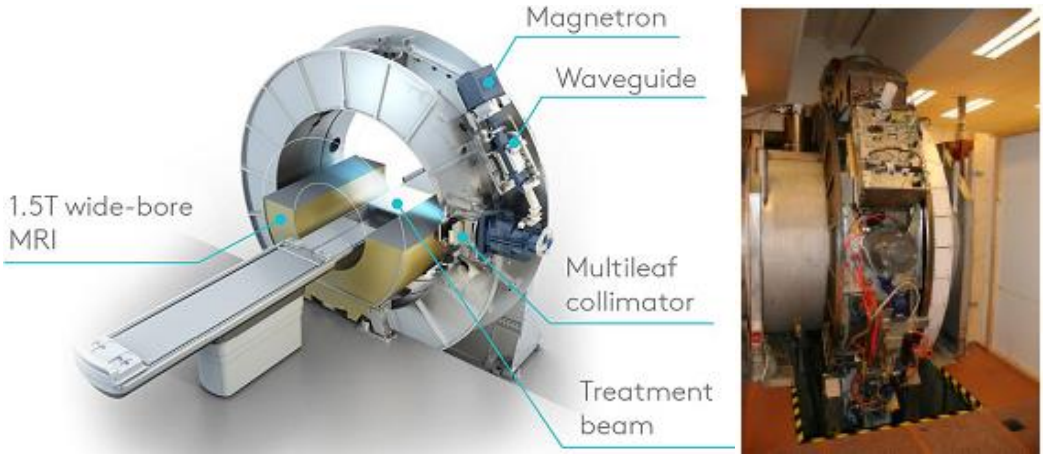

Figure 7. Hybrid MR Imaging and radiation treatment modality (MR-Linac) developed by the University Medical Centre Utrecht: Philips-Elekta. A schematic of MR-Linac (left) and a picture of the prototype set up (right). (Crijnis & Raaymakers, 2014).

The group at the Cross-Cancer Institute has outlined a hybrid system that comprises a 6 MV linac mounted on the open end of a biplanar MRI magnet. Both the linac and magnet positioned on a gantry rotate around the patient. In the first prototype, a 0.2 T MR system with a 27 cm^2 opening coupled with a 6 MV linac was used as a proof of principle (Alberta, 2016). Later in 2013, they upgraded the modality to 0.5 T MRI and a 60 cm diameter opening, shown in **Figure 8**. **Figure 9** shows the commercialized device by University of Alberta and Cross Cancer Institute in Edmonton, Alberta Canada.

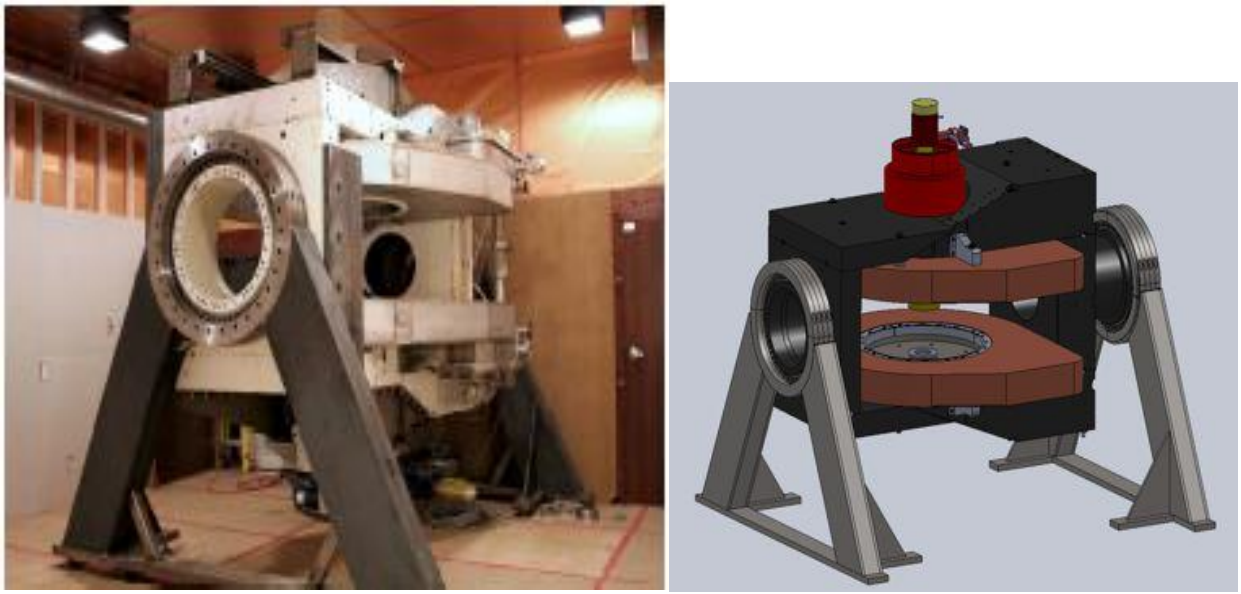

Figure 8. First prototype of the hybrid MR Imaging and radiation treatment modality developed by the Cross Cancer Institute (University of Alberta & Cross Cancer institute, 2013)

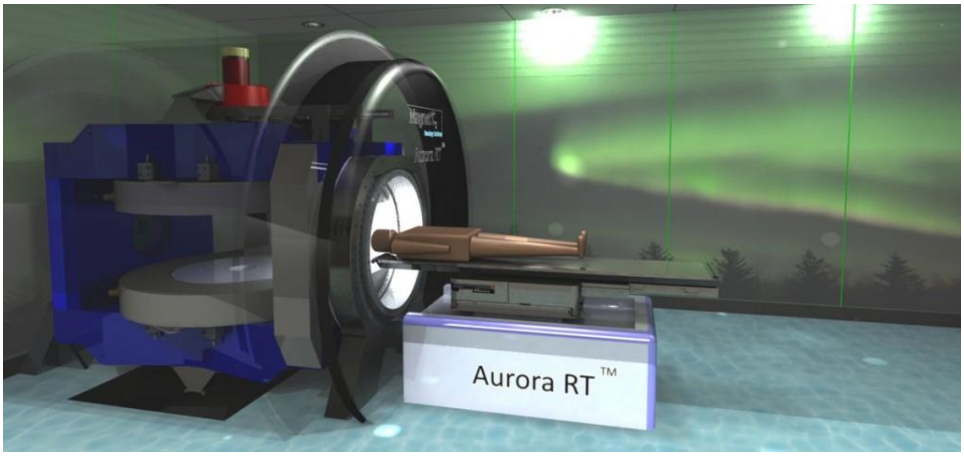

Figure 9. Commercialized MagnetTx oncology solution by University of Alberta and Cross Cancer Institute in Edmonton, Alberta Canada; linac is oriented to be parallel to the magnetic field of the MR unit (MagnetTx Oncology Solutions, 2016).

The MRIdian system has been developed by ViewRay (ViewRay, Ohio, USA). Its combines 3 Cobalt-60 teletherapy heads, with their own multi leaf collimator (MLC) on each, a split-magnet 0.35 T MRI system (Mutic, et al., 2014), shown in Figure 10 (been in clinical use since September, 2014). Moreover, the magnetic flux density affects the radiation dose distribution with radiation detectors, so MRIdian uses magnetic flux density of 0.35 T which is low compared to others i.e. Utrecht: Philips-Elekta MR-Linac with 1.5 T MRI scanner.

The other model proposed by the Australian MRI–Linac program. It is a specifically designed 1 T open-bore MRI/6-MV linac system. The system consists of a fixed horizontal photon beam combined with a MRI.

Since the MRgRT systems are proposed with different orientations of magnetic field with respect to the radiation beam and with different magnetic flux densities, we have carried out simulations in all relevant orientations with magnetic flux density ranging from 0 T to 1.1 T, in this project. **Figure 11** shows the summary of designs proposed by various institutes.

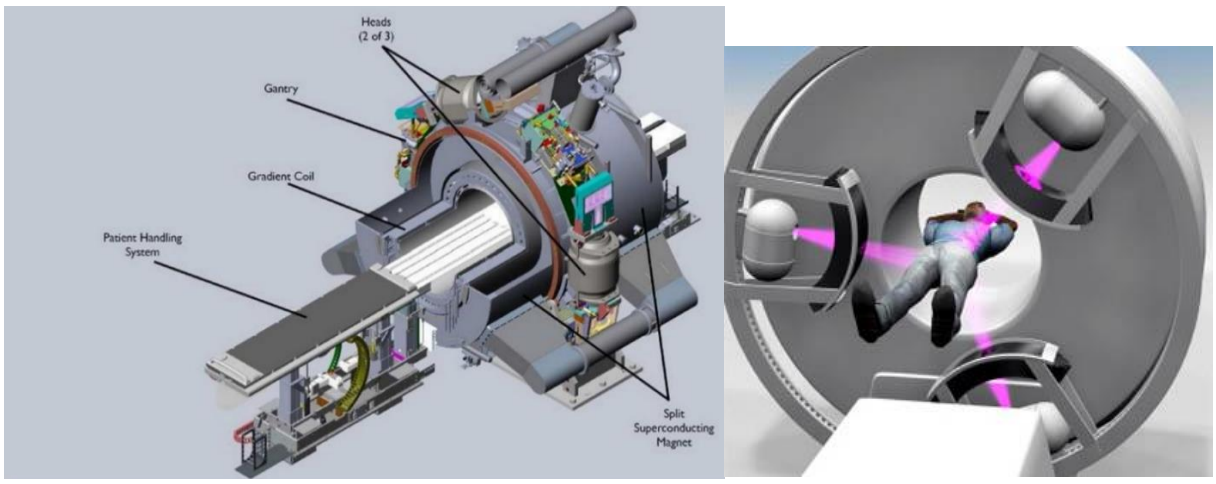

Figure 10. Schematic of ViewRay renaissance system (left image) and model system showing cut-away of beam therapy system (Right image). (Radblog, 2013) (Mutic, et al., 2014).

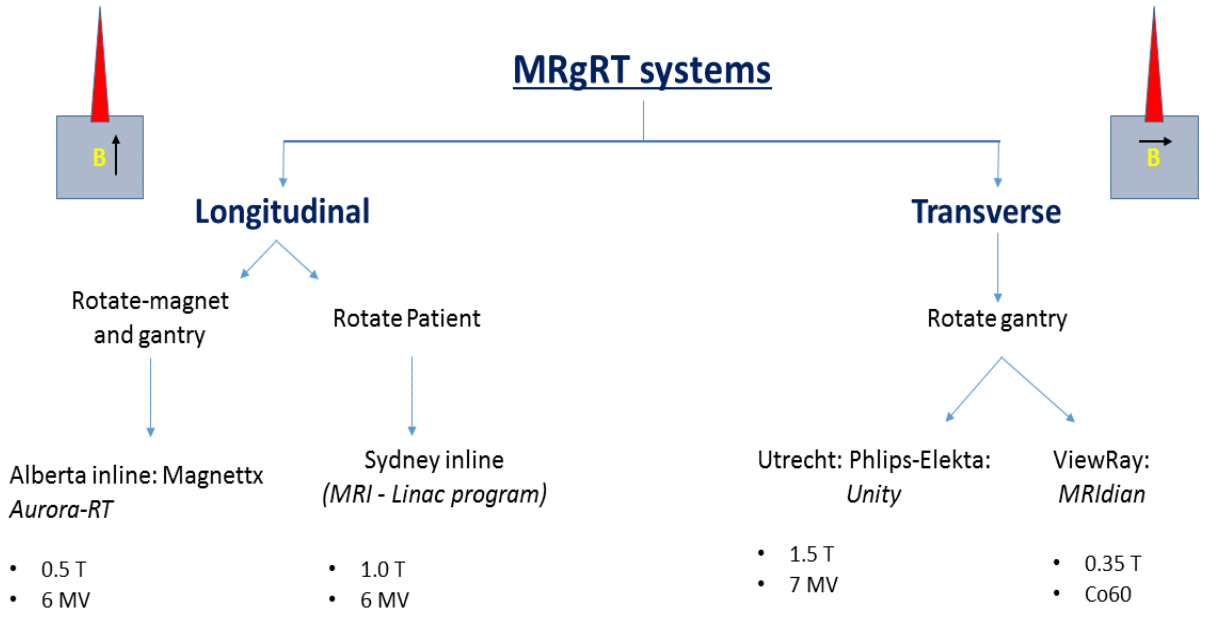

Figure 11. MRgRT systems with their orientation and specification, reproduced from (Oborn, 2016).

2.4.3 Radiation dose and the magnetic field

The integration of an MRI scanner with a radiotherapy unit opens up the opportunity for on-line image guided therapy, and the fact that the isocenters of both integrated devices coincide implies that the radiation is delivered in a magnetic field. The photon beam from the linac is not affected by the magnetic field. However, after the photon interactions with matter a cascade of secondary electrons is released. Under the magnetic field, these moving charged particles will be influenced by the Lorentz force. Electrons in magnetic fields get affected by Lorentz force which is expressed as:

$$\overrightarrow{F_L} = e\vec{v} \times \vec{B} \tag{9}$$

Here, $\vec{v}$ is the electron velocity, $\vec{B}$ is the magnetic flux density, e is the charge.

The electrons are affected with superposition of scatter and deflection by the Lorentz force, resulting in the curved electron tracks (Raaijmakers AJ, 2005). The dose distribution will be affected by the presence of a magnetic field (Raaijmakers AJ, 2007)(Raaijmakers AJ, 2007) (Kirkby C, 2010).

Monte-Carlo simulations have been carried out to investigate the influence of the magnetic field on the dose distribution of a transverse magnetic field of 0.35 T (Reynolds M, 2013) or 1.5 T (Raaijmakers AJ, 2007) (Oborn BM, 2012) or a longitudinal magnetic field (Kirkby C, 2010). The generated electrons in last few centimeters can leave the body in absence of the magnetic field. But under the magnetic field of 1.5 T of MR-Linac, the electron track in air could go up to 180^{o} turn. This causes the electrons to return to the tissue again, depositing its energy, and are so-called electron return effect (ERE) coined by Raaijmakers et al (Raaijmakers AJ, 2005).

2.4.4 Dosimetry in MRgRT

The response of various radiation detection devices as a function of magnetic flux density and the influence of the orientation of magnetic field, beam, and detector for explicit use in MR-linac environment have been characterized by (Reynolds M, 2013) (Reynolds M, 2014) (Smit, et al., 2012) (Smit, et al., 2013) (Smit, et al., 2014) (Meijsing, 2009) (Goddu, et al., 2012) (Raaymakers, et al., 2012). These studies focus on MR-compatible ion chambers with measurements and simulations made in transverse and longitudnal magnetic fields. For reference dosimetry and calibration of various radiotherapy machines, ion chambers are used. Solid state detectors are beneficial due to their small size and their ability to accurately measure dose in small fields (Rustgi & Frye, 1995) (Bucciolini, et al., 2003). But solid state detectors are typically used for relative dosimetry, for example, PDDs or beam profiles. To provide full range of dosimetry options, ionization chambers and various solid state detectors can be used with one another in conjuction.

To our knowledge, the behavior of commercially available chambers have been investigated with respect to magnetic flux densities: PTW30013 Farmer-type ion chamber (Spindeldreier, et al., 2017), NE2571 (Smit, et al., 2013) (Meijsing, 2009) (Reynolds, et al., 2013) and PRO6C (Reynolds, et al., 2013). The response of the NE2571 was measured and showed variations up to 8% to 11%, depending on the orientation of the chamber to the beam (Meijsing, 2009). Monte-Carlo simulations performed with the code Geant4 agreed with measurements within statistical and experimental uncertainties. For the NE2571 chamber, Monte-Carlo simulations with the code PENELOPE were performed and a good agreement within their simulation and measurement uncertatiny with (Meijsing, 2009) was observed. Simulations and measurements differe on average of 0.45%, when the orientation of magnetic field is perpendicular to ion chamber and beam axis. A similar response was observed with the PR06C chamber. The dose response of the PR06C ion chamber, PTW60003 diamond detector and IBA PFD was evaluated in longitudnal orientations, showing little to no effect in response to the magnetic field (Reynolds, et al., 2015).

Measurements and simulations were done with the ionization chamber Farmer NE2571, with magnetic flux density up to1.2 T for measurements and up to 1.5 T for simulations; in two orientations: (a) magnetic field perpendicular to the beam and the chamber axis, (b) magnetic field perpendicular to the chamber axis, but beam parallel to the chamber. The configuration is seen in the **Figure 12**. The path length of electrons in the measurement volume changes the dose distribution for both configurations (Meijsing, 2009).

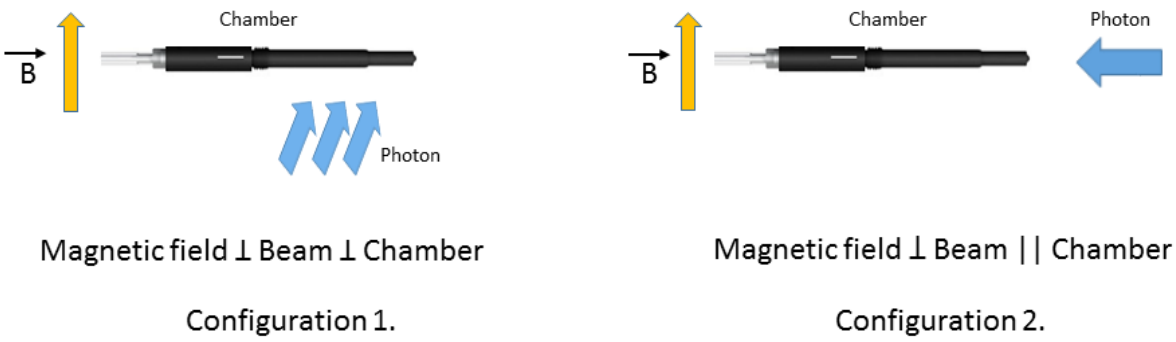

Figure 12. Schematic of orientation of magnetic field with respect to the ionization chamber and beam (Meijsing, et al., 2009).

3. Materials and Methods

This section describes the setup requirements to execute this project. The section is divided into the following main parts; first explaining the apparatus arrangements, second explaining the setup for Monte-Carlo simulation. The third part describes the necessary measurements.

3.1 Experimental Setup

The measurements were carried out using a 6 MV photon beam of a medical linear accelerator (linac, Artíste, Siemens Medical Solutions Inc., PA, USA) and three different ionization chambers placed in a water tank. The experimental electromagnet used can be adjusted to magnetic flux density ranging from 0 to 1.1T.

3.1.1 Magnet system setup

An experimental electromagnet was used for the measurements, having a variable air gap. The magnetic flux density can be regulated by adjusting the distance of the pole shoes and the coil current. For a constant coil current, the larger the distance, the smaller is the magnetic flux density and vice versa. For this project, the pole shoe distance was selected to be 3.5 cm to achieve a maximum magnetic flux density of 1.1 T. While under reference conditions, a field size of 10 x 10 cm^2 is used (IAEA, 2000), the radiation field in the experiment was restricted to 10 x 3 cm^2, to reduce the scattering contribution of the electromagnet. A picture of the electromagnet is shown in **Figure 13** and its specifications are provided **Table 1**. To achieve precise positioning, the magnet is mounted on a trolley, where the height and the vertical position can be adjusted. The magnet is connected to a high voltage power supply that can be controlled from outside the radiation room. In the data sheet (Figure 3.2), the magnetic flux density is shown as a function of the coil current.

The applied currents were calculated for the magnetic flux density range from 0.1 T up to 1.1 T (corresponding to a current of 14.11 A) according to a calculated fit function. **Table 2** shows the calculated and applied current values.

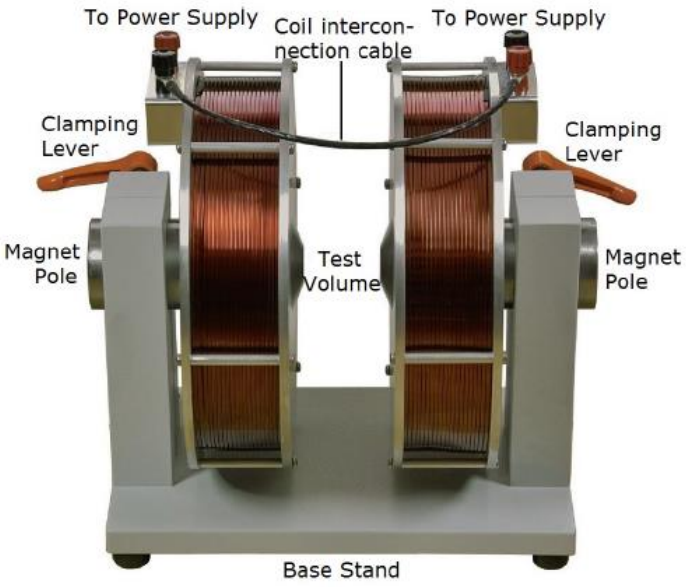

Figure 13. The experimental electromagnet (Messelektronik Schwarzbeck, n.d.)

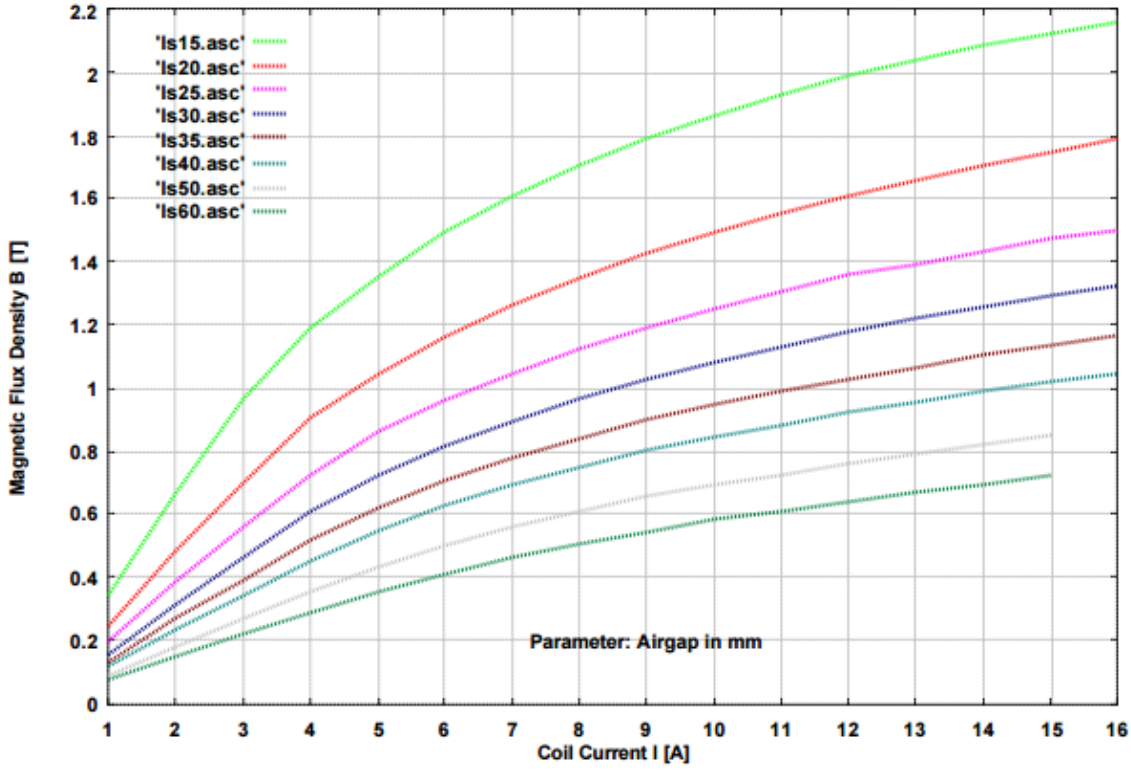

Figure 14. The Magnetic flux density at different air gaps. The air gap used in this project is in maroon color, 'ls35.asc' (Messelektronik Schwarzbeck, n.d., Patent number 5520).

For determining the homogeneity of the magnetic field between the pole shoes, a simulation with the program FEMM (Finite Element Method Magnetics, by David Meeker) had been performed previously (Bakenecker, 2014). The homogeneity in the region where the chambers were positioned is of interest. With a deviation of 1% at most, the field homogeneity is considered sufficient within the measurement volume.

Table 1. Magnet specifications taken from the data sheet (Messelektronik Schwarzbeck, n.d.)

Magnet specifications:	
Number of turns (per coil)	2000
Resistance at room temperature	14 Ω
Maximum coil current	20 A (1 min) 15 A (3 min) 10 A (6 min) 5 A (>20min)
Air gap between pole shoes	0…95 mm
Maximum magnetic flux density	>2.2 T
Coil diameter	33.5 cm
Pole diameter	3 cm
Weight	118 kg
Recommended DC power supply for serial coil operation	250 V / 20 A

Table 2. The magnetic flux density for the specific coil current, taken from the data sheet. (Messelektronik Schwarzbeck, n.d.)

Magnetic flux density (T)	**Coil current (A)**
0.1	0.70
0.2	1.43
0.3	2.20
0.4	3.02
0.5	3.91
0.6	4.89
0.7	6.00
0.8	7.32
0.9	8.96
1.0	11.19
1.1	14.11

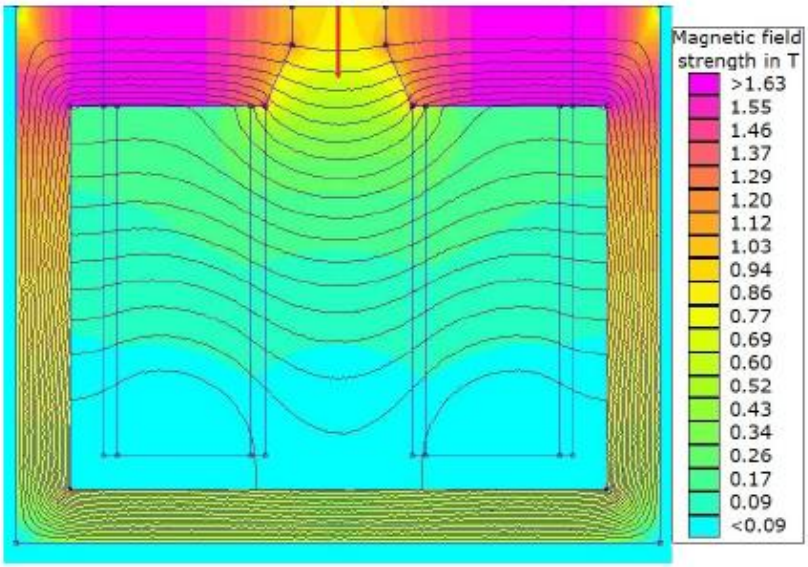

Figure 15. FEMM simulations for the magnetic fields. Simulation results with half of the magnet. Reprinted from (Bakenecker, 2014).

3.1.2 Water tank

The water tank was developed within the Master's project by (Bakenecker, 2014). According to the current IAEA TRS-398 dosimetry protocol (IAEA, 2000), the ionization chambers were placed in 10 cm water equivalent depth for irradiation with 6 MV photons. The tank was printed by a 3D printer using VeroClear RGD 810 as printing material (density of 1.18 – 1.19 g/cm^3). The wall thickness was set to 0.5 cm (at the radiation entrance surface) and the geometrical length of the water tank was 14.82 cm with a surface to measurement point distance of 9.91 cm (equals 10 cm water equivalent thickness). **Figure 16** shows a schematic drawing of the water phantom.

The tank was designed in such a way that the depressions on the sides of the tank fit the dimensions of the pole shoes for a pole shoe distance of 3.5 cm.

Since the electromagnet tends to heat up during the operation, cooling measures need to be taken. Nubs were placed on the sides of the tank to minimize the contact surface between tank and magnet. Additionally, fans were placed at a distance to carry away the heated air from the magnet. Moreover, a water circulation system was integrated in the tank, as shown in **Figure 17**.

Three specific holders were printed, to place the three chambers inside the water tank, exactly in between the pole shoes. **Figure 18** shows the placement of chamber, where the white marker should be facing the source. The chamber positions were important to get consistent measurement.

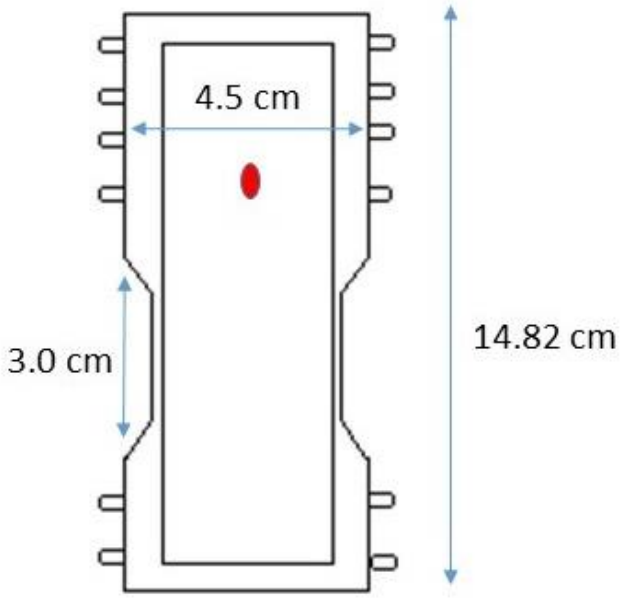

Figure 16. Schematic drawing of the water tank. The red dot indicates the 10 cm water equivalent depth (the position of the ionization chamber).

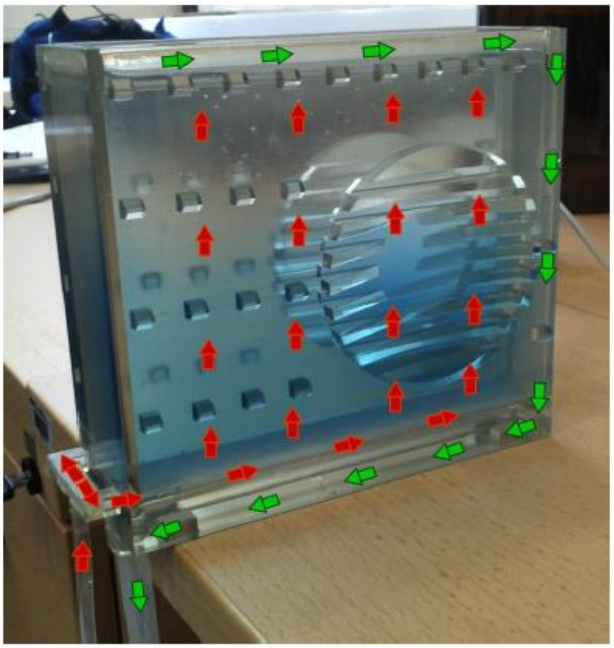

Figure 17. The water flow inside the water tank. Reproduced from (Bakenecker, 2014).

In **Figure 17**, the red arrows show the water pumped up from the bottom to the top through the tank, while the pipes for the water outflow integrated in the tank walls are shown in green arrows. Roof-shaped nubs and grooves on the tank walls are to minimize the contact surface to the magnet.

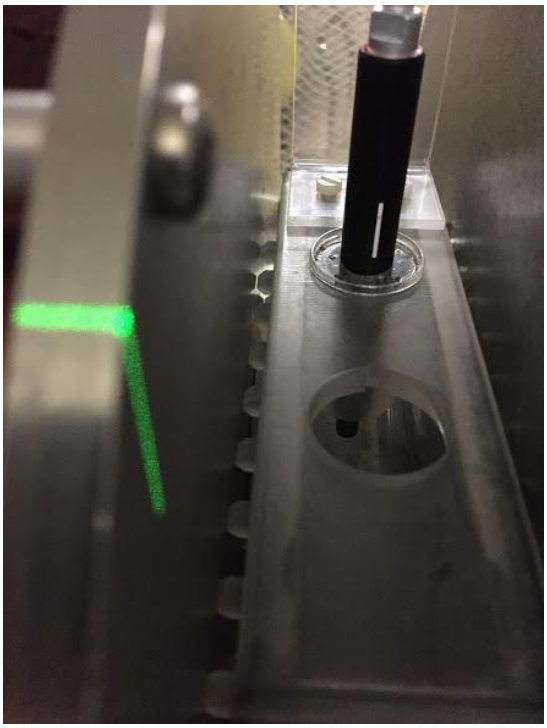

Figure 18. Placement of ionization chamber in water tank.

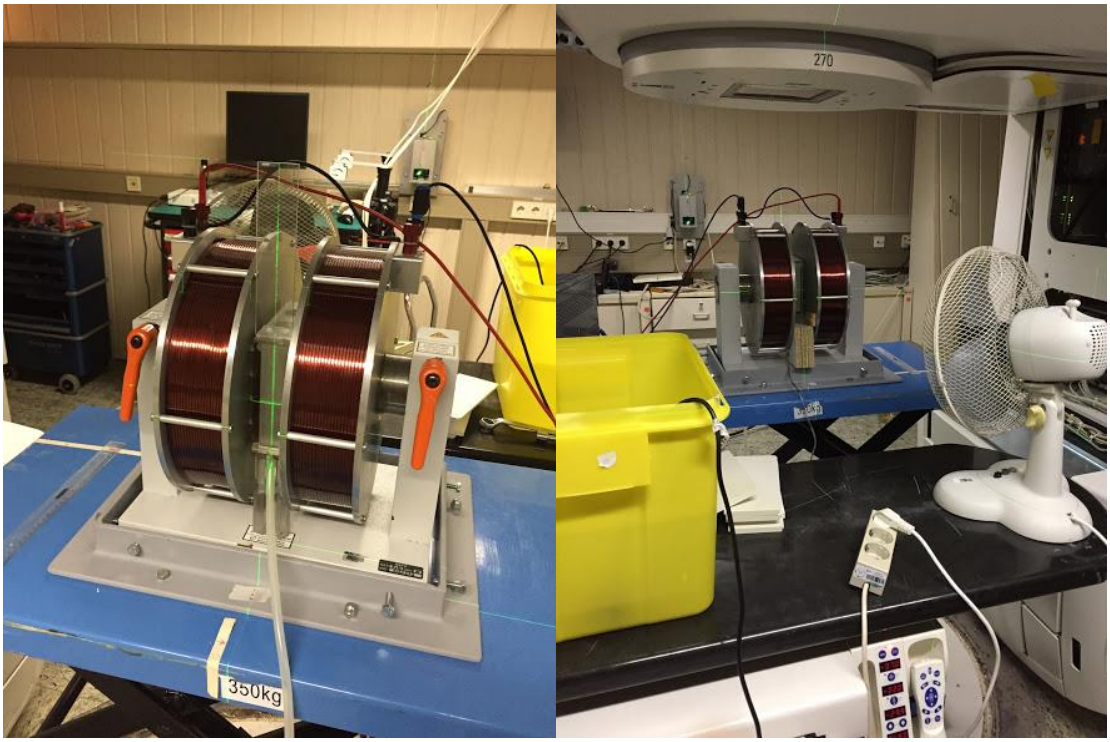

Figure 19. The water tank placed in between the two magnet coils, where the ionization chamber is placed *(Left)*. The fan is placed to carry away the heat that is created by the magnet *(Right)*. The yellow tub on the left is the water reservoir.

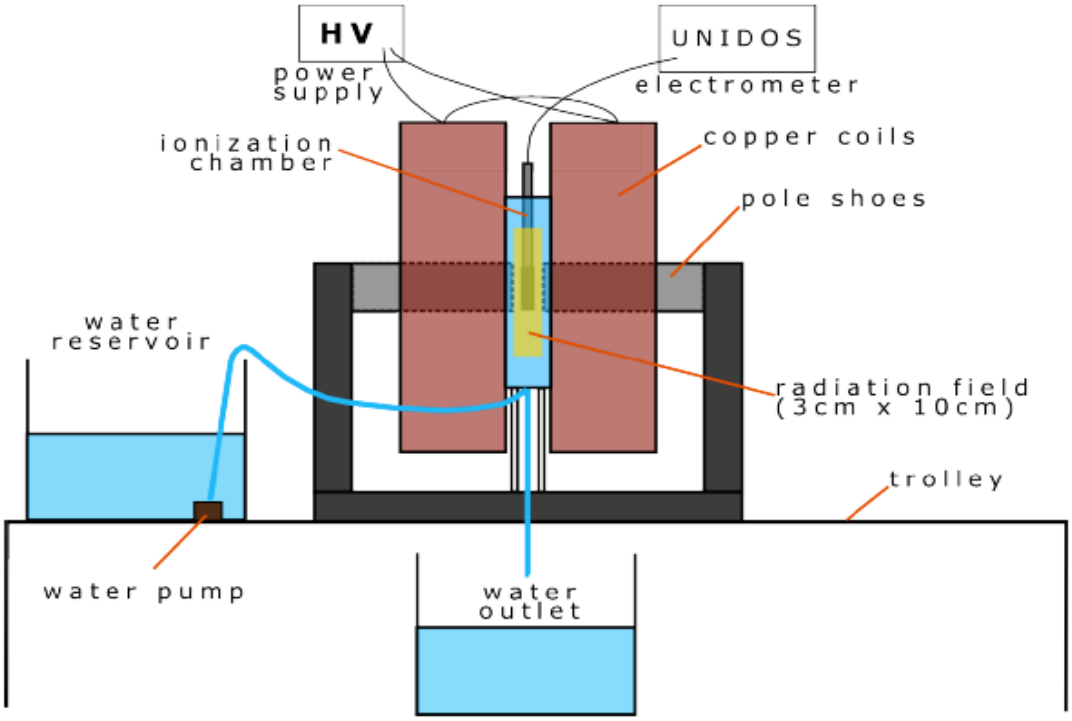

Figure 20. Schematic drawing of the experimental setup. Reproduced from (Bakenecker, 2014).

3.1.3 Ionization chambers

Three different ionization chambers of different cavity sizes were used. The chambers were produced by Standard Imaging Inc. (Wisconsin, USA) and are dedicated MR-compatible (non-ferrous) thimble ionization chambers.

According to the manufacturer (Standard Imaging Inc., 2016), these new MR-compatible ion chambers support the high standard of excellence such as waterproof design, low-leakage, and minimum perturbation. The small volume chambers like A26MR and A1SLMR show unique characteristics like sublinear measurements in magnetic fields with fast settling times and signal stability. The ionizations are measured in units of charge (Coulomb) by an UNIDOS electrometer (PTW, Freiburg, Germany).

The chambers we have used for this project are:

1. Exradin A19MR ion chamber, Farmer type chamber
2. Exradin A26MR ion chamber, Micro chamber
3. Exradin A1SLMR ion chamber, Slimline mini chamber.

The collector, guard and wall are made from C552 air-equivalent plastics, a conductive material. The characteristics of the chambers are shown in the table 3.3.

Table 3. Specifications of the chambers (Standard Imaging Inc., USA).

	A19MR Farmer type chamber	**A26MR Micro chamber**	**A1SLMR Slimline miniature**
Collecting volume	0.62cm^3	0.015 cm^3	0.053 cm^3
Outside diameter of shell collecting volume	7.1 mm	4.3 mm	6.35 mm
Inside diameter of shell collecting volume	6.1 mm	3.3 mm	4.0 mm
Centroid of collecting volume	13.0 mm *(From tip to chamber)*	1.98 mm *(From tip to chamber)*	4.1 mm *(From tip to chamber)*
Shell wall thickness	0.5 mm	0.5 mm	1.1 mm
Collector diameter	1.0 mm	0.75 mm	1.0 mm
Collector length	21.6 mm	1.78	4.4 mm
Shell/Entry window, collector and guard material	C552 *(Shonka air-equivalent plastic)*	C552 *(Shonka air-equivalent plastic)*	C552 *(Shonka air-equivalent plastic)*

Figure 21. The ion chambers used for this project. Left to right: A19MR ion chamber, A1SLMR ion chamber and A26MR ion chamber.

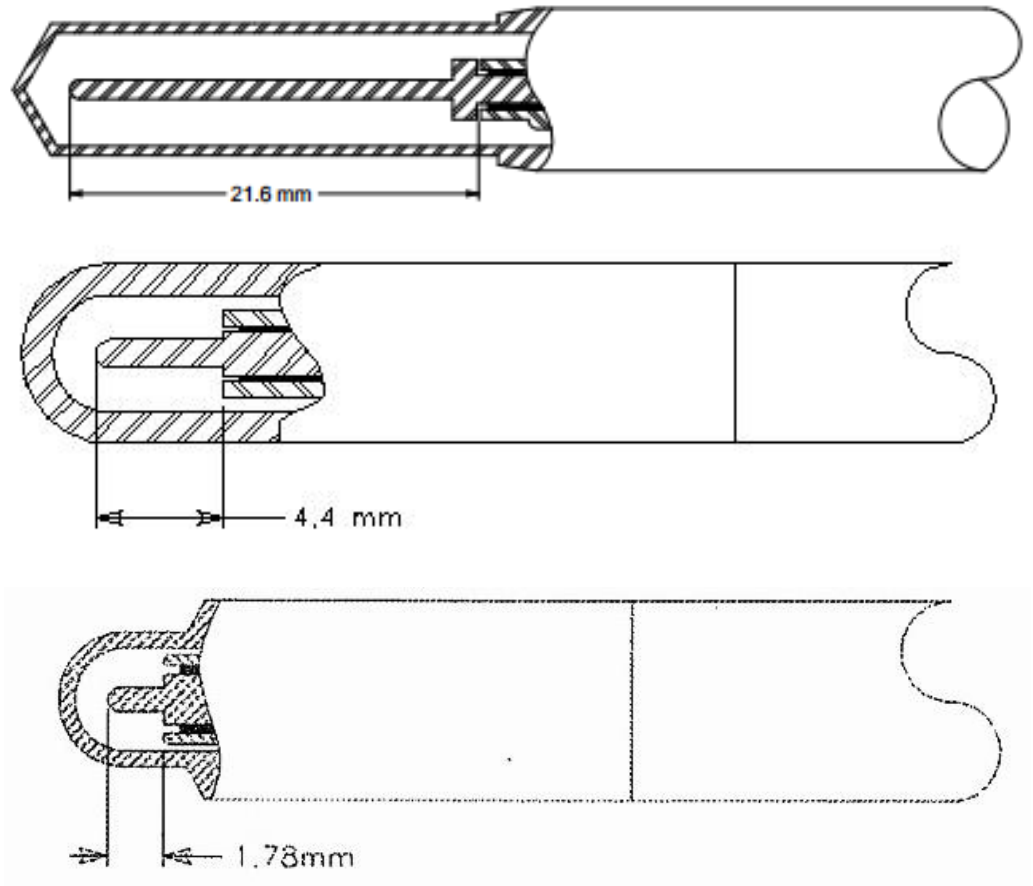

Figure 22. Schematic drawing of the ionization chambers (top to bottom): A19MR Farmer-type ion chamber with collecting volume 0.62 cc, A1SLMR slimline miniature ion chamber with collecting volume 0.053 cc, and A26MR ion chamber micropoint with collecting volume of 0.015 cc. (Standard Imaging Inc., 2016).

3.2 Simulation Setup

3.2.1 EGSnrc

The Monte-Carlo code EGSnrc was used for simulation of the ion chambers. This code was chosen as it is an efficient code for simulation of photon/electron transport in the energy range needed for dosimetry, and is benchmarked against measurements. EGSnrc uses an exact boundary-crossing algorithm, where elastic scattering events are simulated individually in the environment of interfaces between different materials.

EGSnrc was configured for the particular simulation environment on the computer. Additional programs were used such as egs_view to visualize the simulation geometry. All the orientations of magnetic field with ion chamber are simulated using EGSnrc egs++ user code egs_chamber. Each simulation was done with 8 x $10^8$the histories, in order to determine the uncertainty of simulation below 0.1%.

The total energy deposition inside the sensitive cavity of ionization chamber is scored as a function of magnetic field. The chamber response for all orientations and magnetic flux density are normalized to the case of 0 T. The relative response is compared with the measurements.

EGSnrc includes many new features compared to EGS4. The default settings of the system allow the most complete and accurate simulation of the interaction processes which EGSnrc is capable of. There is a possibility that, in some cases this may result in overkill and reduction in efficiency without gaining accuracy (e.g. when the atomic relaxation or bound Compton scattering is included for high energy photon calculations). In EGSnrc, the user has the ability to switch parameters on or off by setting a flag. In the same manner, the user can choose to model Klein Nishina Compton scattering (free electrons) instead of bound Compton scattering.

For the transport parameters, there is the choice of ON, OFF, SIMPLE or NOREJ for bound Compton scattering. If OFF is used, Compton scattering is treated as Klein-Nishina. If ON is used, Compton scattering is treated with impulse approximation. With the use of SIMPLE, the impulse approximation incoherent scattering function is used (i.e. no Doppler broadening). If it is set to NOREJ, the actual total bound Compton cross sections are used and there are no rejections at run time. Simple and Norej are the new options added for Compton scattering in EGSnrc. For this thesis Bound Compton scattering was used, i.e. Compton scattering parameter is set to NOREJ.

3.2.2 Modelling of the chambers

According to the technical data specifications provided by Standard Imaging Inc. and image results from micro computed tomography (micro-CT) of the chambers, all the ionization chambers were modelled with the egs++ library (Kawrakow, 2006).

The micro-CT was carried out with Inveon PET·SPECT·CT (Siemens, Erlangen, Germany). The results from the micro-CT were processed on the open source software "3D Slicer" (Slicer 4.6) (Fedorov, et al., 2012), a platform for medical informatics, image processing and three-dimensional visualization. With the help of 3D Slicer, the chamber geometries were studied in detail. **Figure 23**, **Figure 24** and **Figure 25** show the micro-CT results of the chambers A19MR, A1SLMR, and A26MR, respectively.

Modelling of the A19MR ion chamber

The A19MR ionization chamber is modelled as an air cavity with a diameter and length of 6.1 mm and 24.1 mm, respectively, surrounded by C552 material cylinder with a wall thickness of 0.5 mm. One end of the chamber is conical top of 2.1 mm high. In the air cavity, C552 central electrode is modelled with diameter and length of 1.0 mm and 21.8 mm, respectively. A sensitive volume of 0.62 cm^3 consists both of air cavity and central electrode.

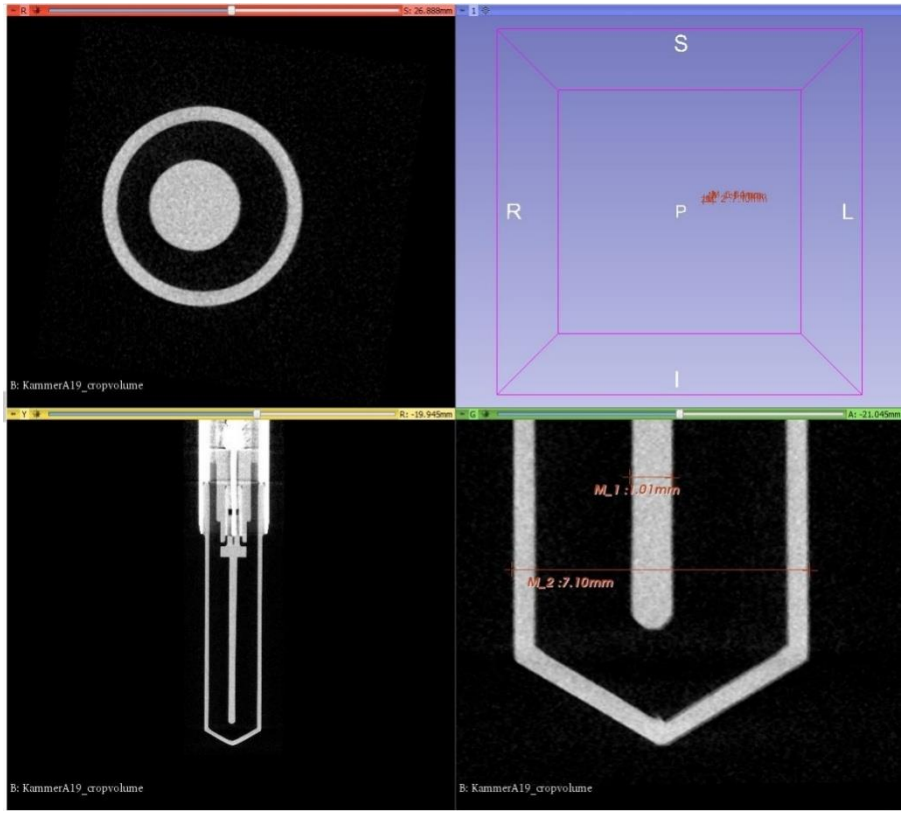

Figure 23. Micro-CT image of A19MR ionization chamber.

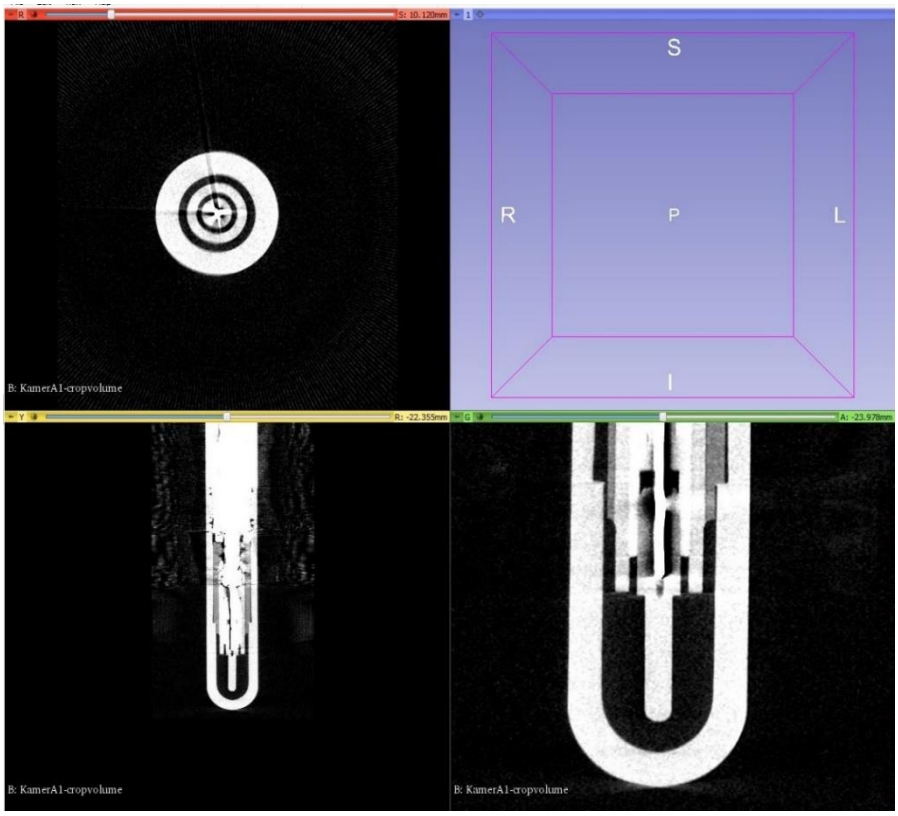

Figure 24. Micro-CT image of A1SLMR ionization chamber.

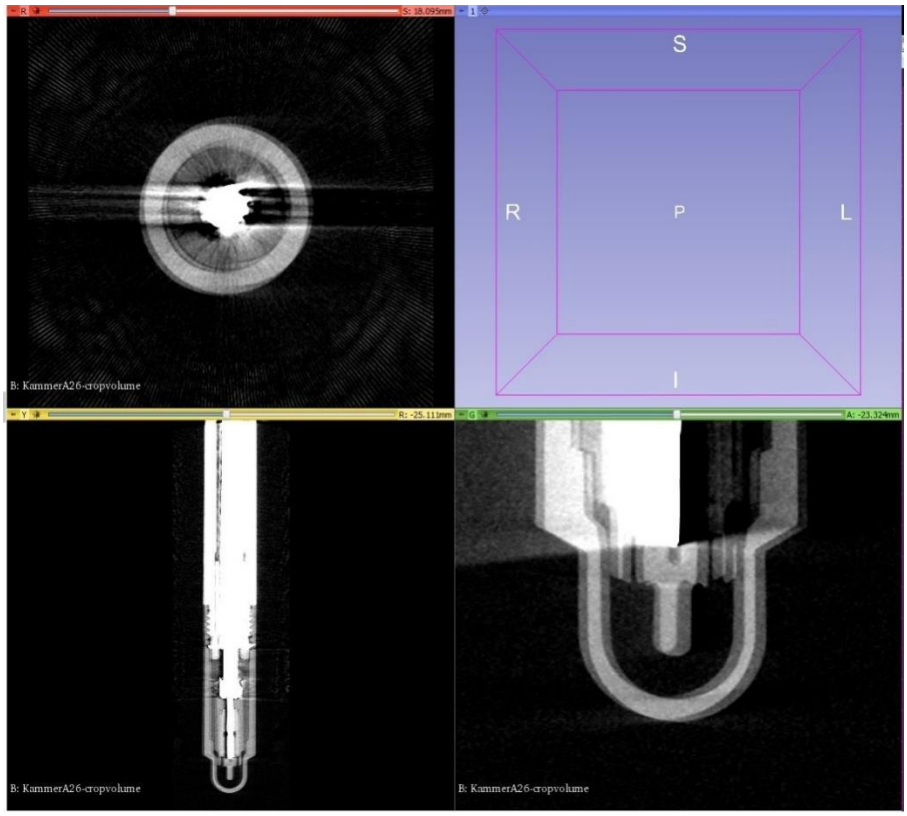

Figure 25. Micro-CT image of A26MR ionization chamber.

Modelling of the A1SLMR ion chamber

Totally different geometry as compared to A19MR ionization chamber. The A1SLMR ionization chamber is modelled as an air cavity with a diameter and length of 4.0 mm and 6.86 mm, respectively, surrounded by C552 material cylinder with a wall thickness of 1.1 mm. One end of the chamber is hemispherical top of 3.5 mm radius. In the air cavity, C552 central electrode is modelled with diameter and length of 1.0 mm and 4.4 mm, respectively. A sensitive volume of 0.053 cm^3 consists both of air cavity and central electrode.

Modelling of the A26MR ion chamber

Similar geometry to A1SLMR, but micropoint chamber with diameter and length of 3.3 mm and 3.88 mm, respectively, surrounded by C552 material cylinder with a wall thickness of 0.5 mm. One end of the chamber is hemispherical top of 2.1 mm radius. In the air cavity, C552 central electrode is modelled with diameter and length of 1.78 mm and 0.37 mm, respectively. A sensitive volume of 0.015 cm^3 consists both of air cavity and central electrode.

The surroundings of the ionization chamber can be interpreted and modelled as homogeneous water. The materials were defined in the PEGS4 files to develop the model. In the cross-section library PEGS4 (e.g., H2O521ICRU) is already defined as the default material for simulations of the absorbed dose to water for the ionization chamber model materials.

For the simulation, there were several variance reduction techniques employed as mentioned in section 2.3.4. An additional geometry encapsulating the basic model in a 1 cm thick shell was made to employ XCSE (photon cross-section enhancement). Moreover, Russian roulette of charged particles is done in a way that some of the time constrains from examining the particles stage space unless it survives.

3.2.3 Input file progression

The egs_chamber user code was utilized in conjunction with a set of information to model the chamber for simulation. These directions are gathered in a file called an input file which is passed to egs_chamber user code at runtime alongside with a material file. Each input record comprises of a several sections of particular instructions giving important definitions such as geometry, source, and run control, scoring options, calculations, variance reduction and Monte-Carlo transport parameters.

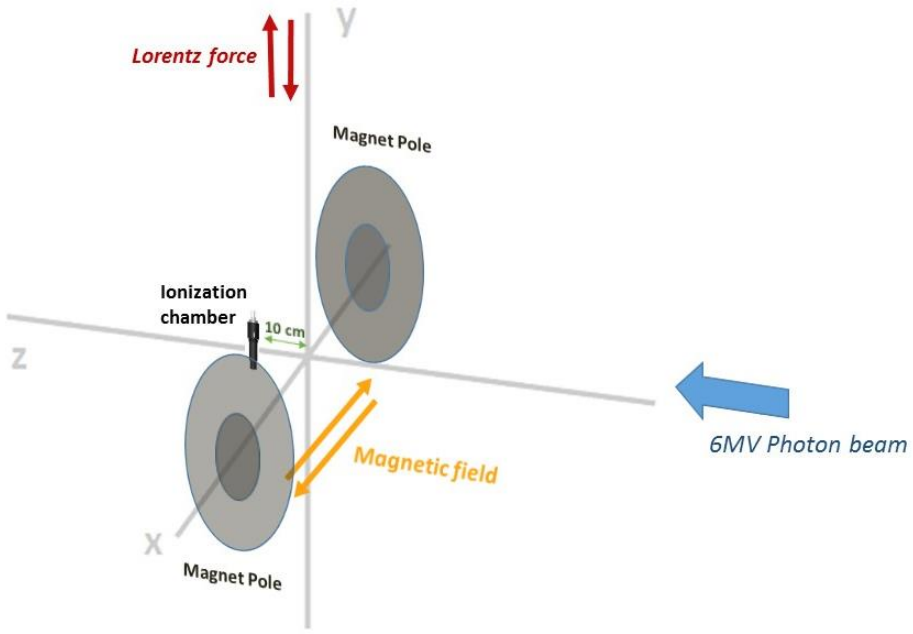

Figure 26. Setup with magnetic field perpendicular to ion chamber and the photon beam; magnetic field in X-direction of 3D Cartesian system. Experimental setup was possible in this orientation only.

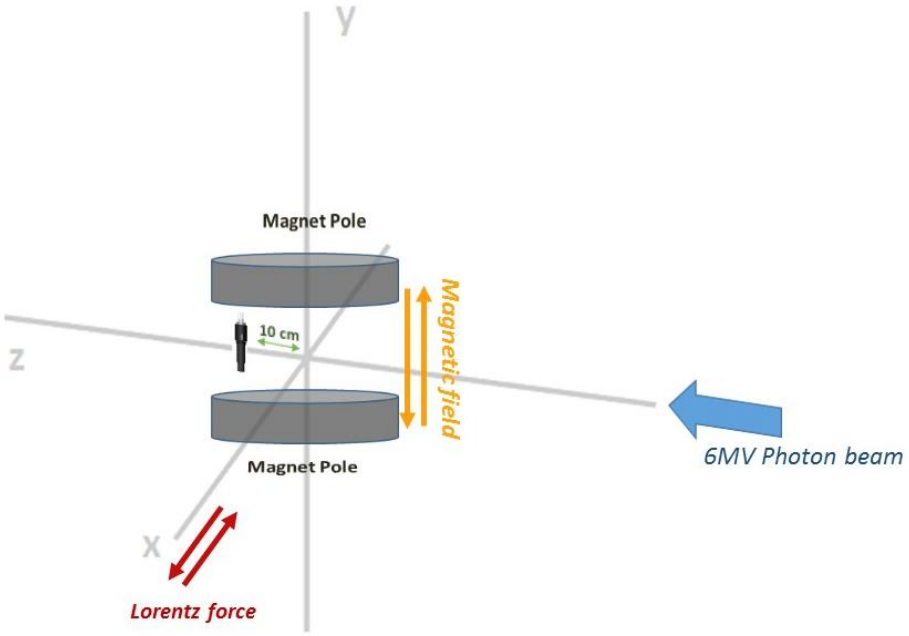

Figure 27. Setup with magnetic field perpendicular to the beam, parallel to chamber; magnetic field in Y-direction of 3D Cartesian system.

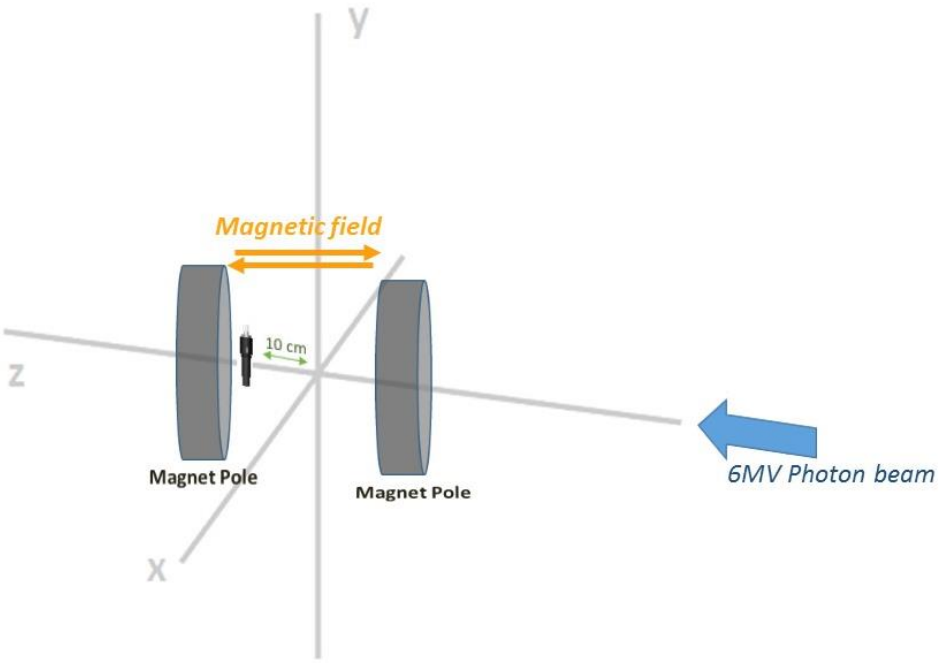

Figure 28. Setup with magnetic field parallel to the beam and perpendicular to the ion chamber, magnetic field in Z-direction of 3D Cartesian system.

During this project, in total 72 input files were developed for each chamber. The chamber response to a 6 MV photon beam (Mohan, et al., 1985) (For detailed information, in secton 5) magnetic flux density ranging from 0 T to 1.1 T, aligned perpendicular to the chamber and beam axis for each ion chamber. In this project, we have mentioned the magnetic field direction with respect to the virtual planes, X, Y and Z direction. In simple manner, for every magnetic flux density (0.0 T to 1.1 T) a positive and negative direction was assigned in X, Y and Z direction.

3.3 Charge measurements with ionization chambers

The cavity of ionization chamber is filled with air, whose mass in the sensitive cavity of the chamber is equal to the product of the density of the air and effective volume of the chamber. Since most of the ionization chambers are in contact to the ambient air, the density of the air is function of the atmospheric temperature and pressure. Hence, the constant check of the temperature and pressure is essential, as the ionization chambers are sensitive to a change in the room atmosphere. Temperature measurements were carried out by means of an electric thermometer. During each set of measurements, the temperature of the water inside the phantom was measured. Also, the pressure inside the experimental room was measured using a barometer.

Since an electromagnet was used, the polarity can be reversed. The measurements were also carried out by altering the polarity of pole shoes, in order to investigate the behavior of chamber

response for a magnetic field in both directions. A hall-probe was used to verify the direction of the magnetic field.

The water tank was positioned between the pole shoes of the electromagnet according to the laser markers of the linac. The radiation field size was set at 3 cm x 10 cm with the radiation entrance surface placed in the isocenter at a distance of 100 cm to the source.

Measurements were carried out three times for each chamber. Zeroing of the PTW electrometer was done prior to each set of the measurements. Moreover, the ionization chambers were pre-radiated with 300 MU in the absence of the magnetic field (according to the recommendations of IAEA [2000]). Later, all the measurements were carried out with 100 MU.

Each ionization chamber was irradiated in the presence of a magnetic field ranging from 0 T to 1.1 T, while the order of magnetic flux density was randomized. The motive to measure at random order of magnetic flux density was to statistically avoid hysteresis effects. In the electromagnet, the current was set according to the **Table 2**.

4. Results and Discussion

4.1 Experimental measurements

As mentioned in the experimental setup 3, the measurements produced here are in charge (Coulomb). As mentioned in 3.3, the sequential measurement was carried out three times for each chamber. Each ionization chamber was irradiated under magnetic flux density ranging from 0 T to 1.1 T, while the order of magnetic flux density was randomized to avoid hysteresis effects.
To be noted, the experimental measurements were only possible for the orientation:
The beam is perpendicular to the magnetic field and the chamber axis. (Orientation I). The electrometer displayed the result with four digits.

The following tables show the experimental measurements.

Table 4. A19MR Ionization chamber. Table shows the mean charge of three measurements and the standard deviation (Magnetic field towards + X direction).

Magnetic flux density (T)	Mean charge (nC)	Standard deviation (nC)
0.0	12.11	0.02
0.1	12.19	0.01
0.2	12.29	0.01
0.3	12.45	0.02
0.4	12.62	0.02
0.5	12.78	0.02
0.6	12.93	0.02
0.7	13.03	0.01
0.8	13.09	0.02
0.9	13.12	0.01
1.0	13.12	0.02
1.1	13.10	0.02

Voltage: +300 V

Temperature: 22^{o} C

Pressure: 985.6 mbar

Table 5. A19MR Ionization chamber. Table shows the mean charge of three measurements and the standard deviation (Magnetic field towards - X direction).

Magnetic flux density (T)	Mean charge (nC)	Standard deviation (nC)
0.0	12.09	0.01
0.1	12.09	0.01
0.2	12.15	0.01
0.3	12.27	0.01
0.4	12.42	0.01
0.5	12.58	0.01
0.6	12.71	0.01
0.7	12.79	0.01
0.8	12.85	0.01
0.9	12.89	0.02
1.0	12.89	0.02
1.1	12.87	0.01

Voltage: +300 V

Temperature: 22.25^{o} C

Pressure: 985.1 mbar

Table 6. A1SLMR Ionization chamber. Table shows the mean charge of three measurements and the standard deviation (Magnetic field towards + X direction).

Magnetic flux density (T)	Mean charge (nC)	Standard deviation (nC)
0.0	1.009	0.001
0.1	1.013	0.001
0.2	1.018	0.001
0.3	1.024	0.001
0.4	1.029	0.001
0.5	1.034	0.001
0.6	1.038	0.001
0.7	1.041	0.000
0.8	1.043	0.001
0.9	1.045	0.001
1.0	1.045	0.001
1.1	1.046	0.001

Voltage: +300 V

Temperature: 23.10^{o} C

Pressure: 980.1 mbar

Table 7. A1SLMR Ionization chamber. Table shows the mean charge of three measurements and the standard deviation (Magnetic field towards - X direction).

Magnetic flux density (T)	Mean charge (nC)	Standard deviation (nC)
0.0	1.011	0.001
0.1	1.008	0.000
0.2	1.004	0.001
0.3	1.002	0.001
0.4	1.001	0.000
0.5	1.000	0.000
0.6	1.000	0.001
0.7	1.001	0.001
0.8	1.002	0.001
0.9	1.004	0.001
1.0	1.005	0.001
1.1	1.006	0.000

Voltage: +300 V

Temperature: 22.60^{o} C

Pressure: 981.3 mbar

Table 8. A26MR Ionization chamber. Table shows the mean charge of three measurements and the standard deviation (Magnetic field towards +X direction).

Magnetic flux density (T)	Mean charge (pC)	Standard deviation (pC)
0.0	328.7	0.3
0.1	329.9	0.4
0.2	330.7	0.1
0.3	331.6	0.4
0.4	331.9	0.2
0.5	332.0	0.5
0.6	332.4	0.2
0.7	332.3	0.2
0.8	332.2	0.1
0.9	332.1	0.1
1.0	331.6	0.3
1.1	331.1	0.1

Voltage: +300 V

Temperature: 23.10^{o} C

Pressure: 981.3 mbar

Table 9. A26MR Ionization chamber. Table shows the mean charge of three measurements and the standard deviation (Magnetic field towards - X direction).

Magnetic flux density (T)	Mean charge (pC)	Standard deviation (pC)
0.0	329.1	0.1
0.1	328.1	0.1
0.2	327.2	0.2
0.3	326.4	0.2
0.4	325.6	0.3
0.5	325.0	0.1
0.6	324.4	0.1
0.7	323.9	0.1
0.8	323.6	0.2
0.9	323.4	0.1
1.0	323.2	0.2
1.1	323.0	0.1

Voltage: +300 V

Temperature: 23.15^{o} C

Pressure: 980.1 mbar

4.2 Simulation results

The input files of the developed chamber models for the EGSnrc code were executed in a UNIX-like environment. The progression of batch scripts that enabled continuous simulations to be run on several cores (computing cluster) and in direct succession proved to be vital with respect to the target histories number, the number of orientations simulated and the time available.

All models developed are approximations. In Monte-Carlo simulations, several factors (the number of histories simulated, the photon transport system etc.) affect the accuracy. So, the simulations were carried out with 8 x 10^8 histories, to achieve an uncertainty of about 0.1%.

Figure 29 shows the simulation geometry of the experimental setup. The chamber is positioned at 10 cm on the Z axis according to the protocol IAEA TRS-398, in a water phantom. In the right figure the opacity of water is turned off, revealing the green outer surface of the chamber, which is PEGS material C552ICRU (Shonka, air equivalent material).

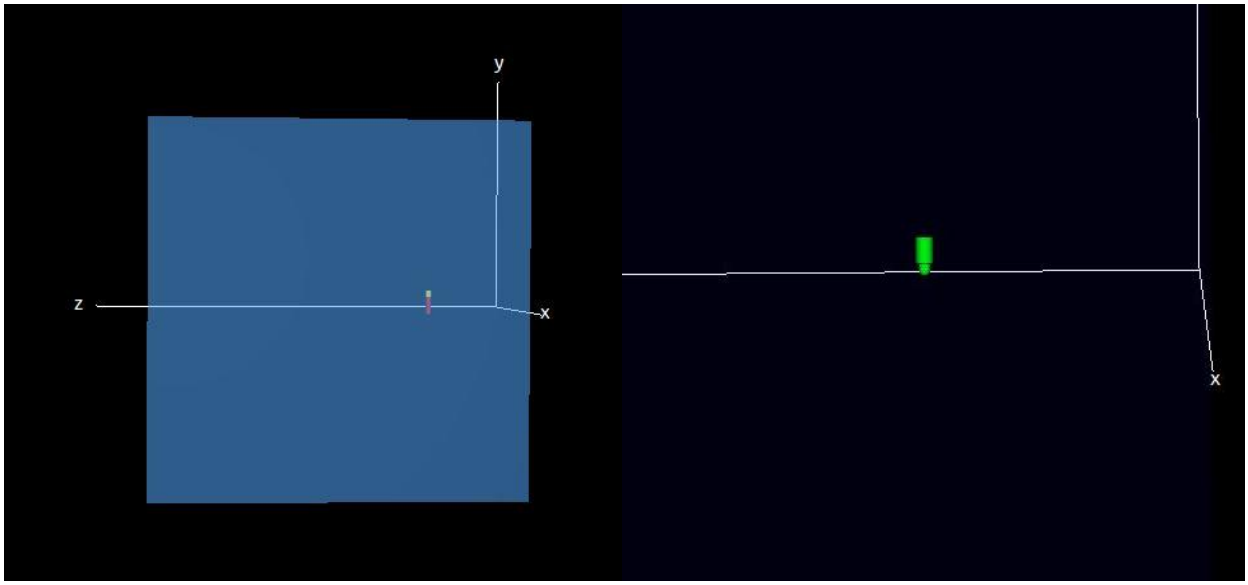

Figure 29. The chamber position in the water phantom in blue color *(Left)*. The closer view of chamber positioned at 10 cm on z-axis *(Right)*.

The results are derived in relative values. The propagation of error was calculated to determine the uncertainty of the results obtained from multiple variables in simulation. The relative errors are shown in all the plots with error bars on each data.

Since the experimental setup was practically possible only for the orientation I; the magnetic field perpendicular to the beam and the chamber axis, the experimental and simulation results for the the chambers A19MR, A1SLMR, A26MR are shown in the same plot in **Figure 30**, **Figure 33**, **Figure 36**, respectively.

Figure 31, **Figure 34** and **Figure 37** show the simulation results for the orientation II, the magnetic field parallel to the chamber axis and perpendicular to the beam axis. **Figure 32**, **Figure 35** and **Figure 38** show the results for the orientation III, the magnetic field perpendicular to the chamber axis and parallel to the beam axis. The plots also show the result for reversed magnetic field polarity, mentioned with '+' or '-'direction of the Cartesian plane.

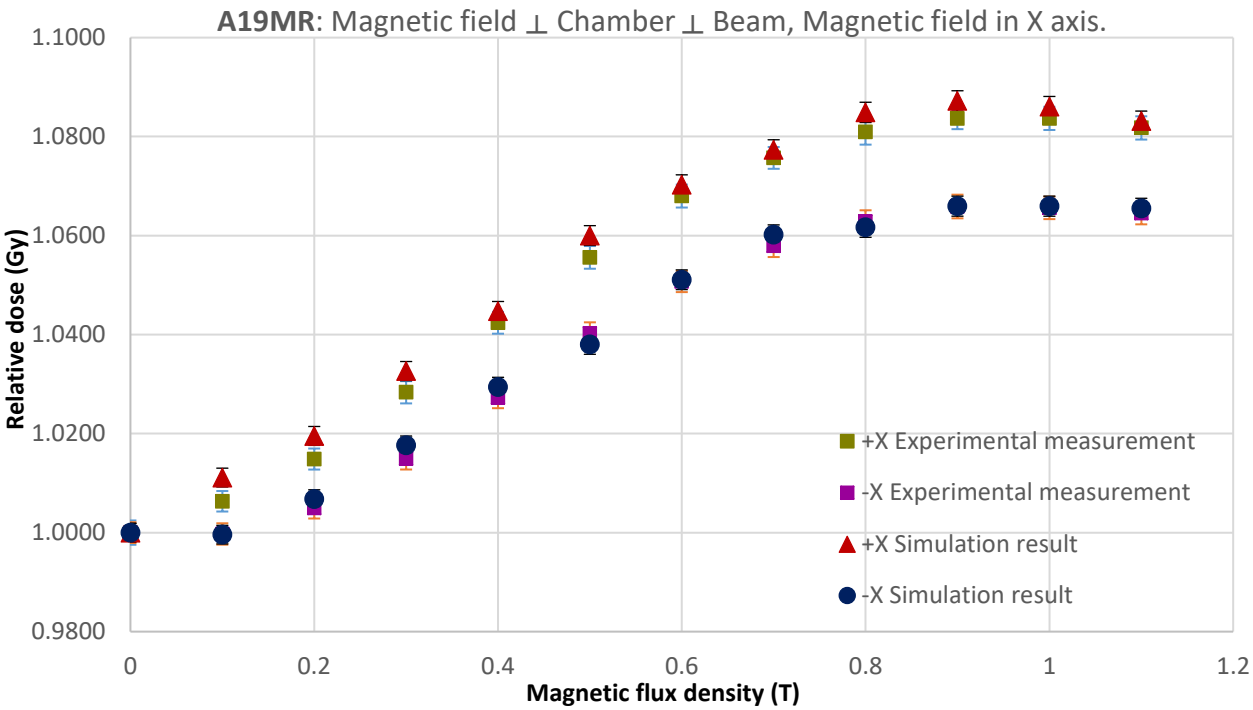

Figure 30. A19MR ionization chamber (Configuration I); the experimental and simulation measurements in X direction. The error bars on each data show the relative uncertainty.

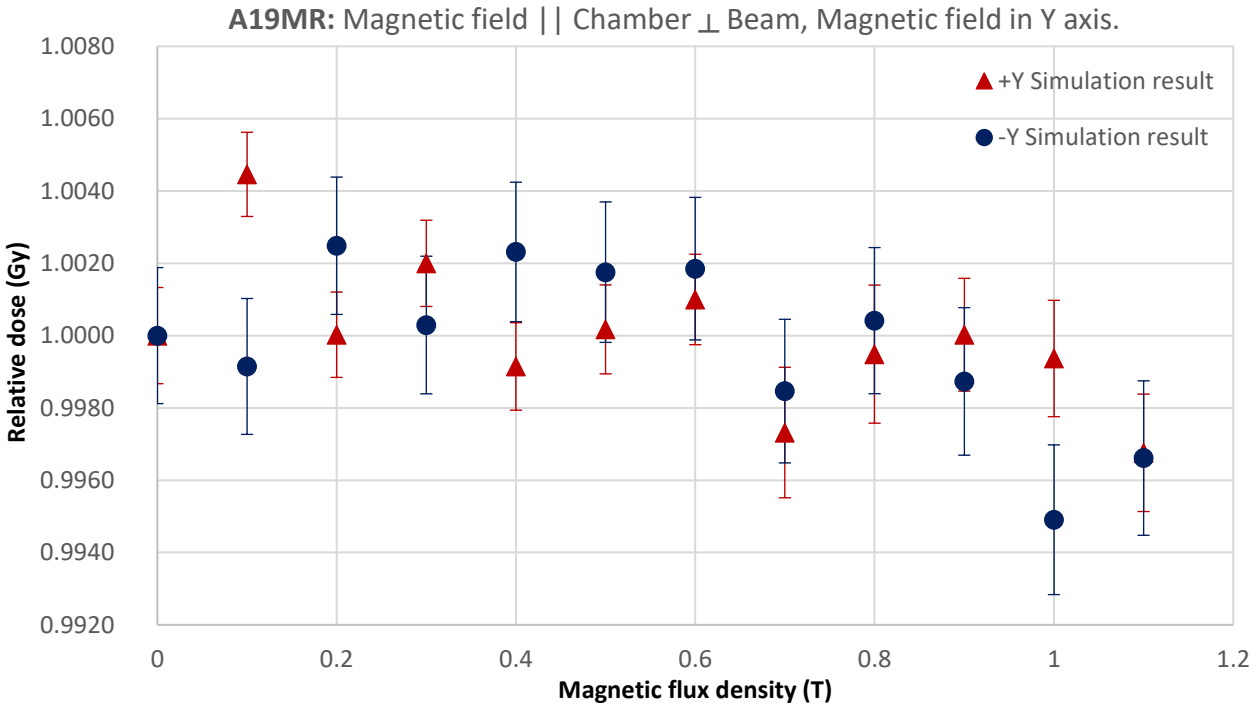

Figure 31. A19MR ionization chamber (Orientation II); the simulation measurements in Y direction. The error bars on each data show the relative uncertainty.

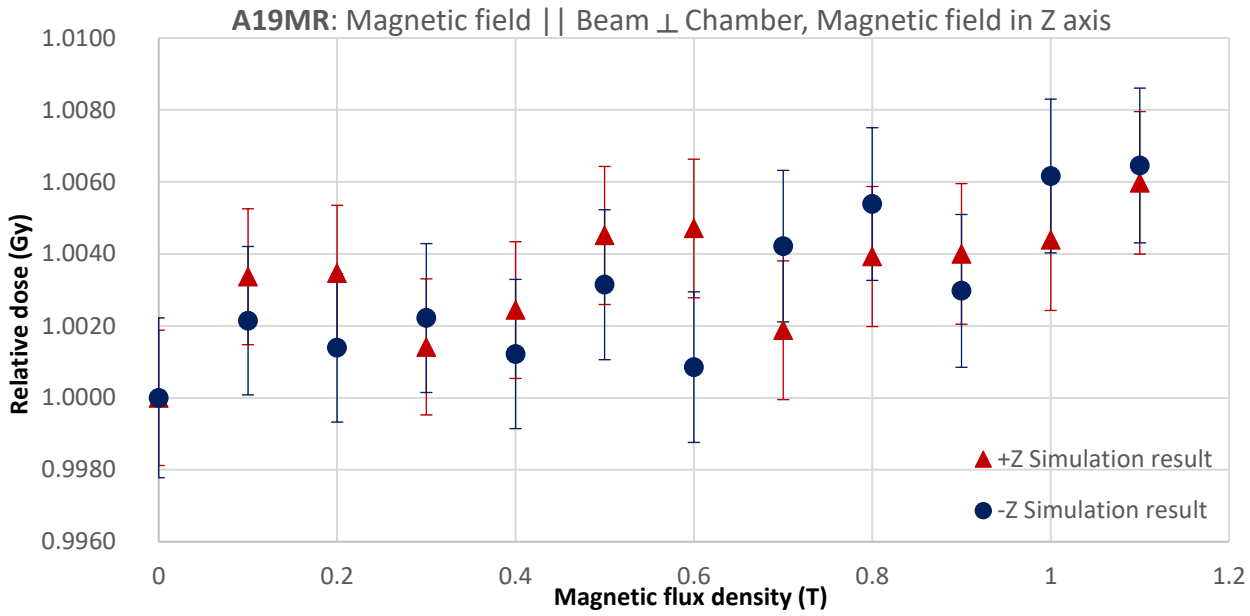

Figure 32. A19MR ionization chamber (Orientation III); the simulation measurements in Z direction. The error bars on each data show the relative uncertainty.

A19MR ionization chamber

The plot for orientation I, compares the Monte-Carlo simulation and measurements and shows a very good agreement with each other. The chamber response increases slowly to a maximum of 1.085 at 0.9 T before decreasing towards 1.0 at higher magnetic flux density. Reversing the magnetic field direction yields a maximum increase of 1.065 at 0.9 T. The statistical uncertainty of the simulation remains below 0.20%.

For orientation II, the simulation shows no appreciable chamber response to the magnetic flux density. The calculated response in both polarities varied in between 0.995 and 1.005, which is within ±0.5% of the value without magnetic field. That is very little change in response with magnetic flux densities. The statistical uncertainty of the simulation remains below 0.21%.

For orientation III, the simulation results in both polarities varied between maximum 1.007 at 1.1 T and lowest 1.000 at 0 T with unpredictable response with respect to the magnetic flux densities. The response shows an increase of 0.7%. The statistical uncertainty of the simulation remains below 0.22%.

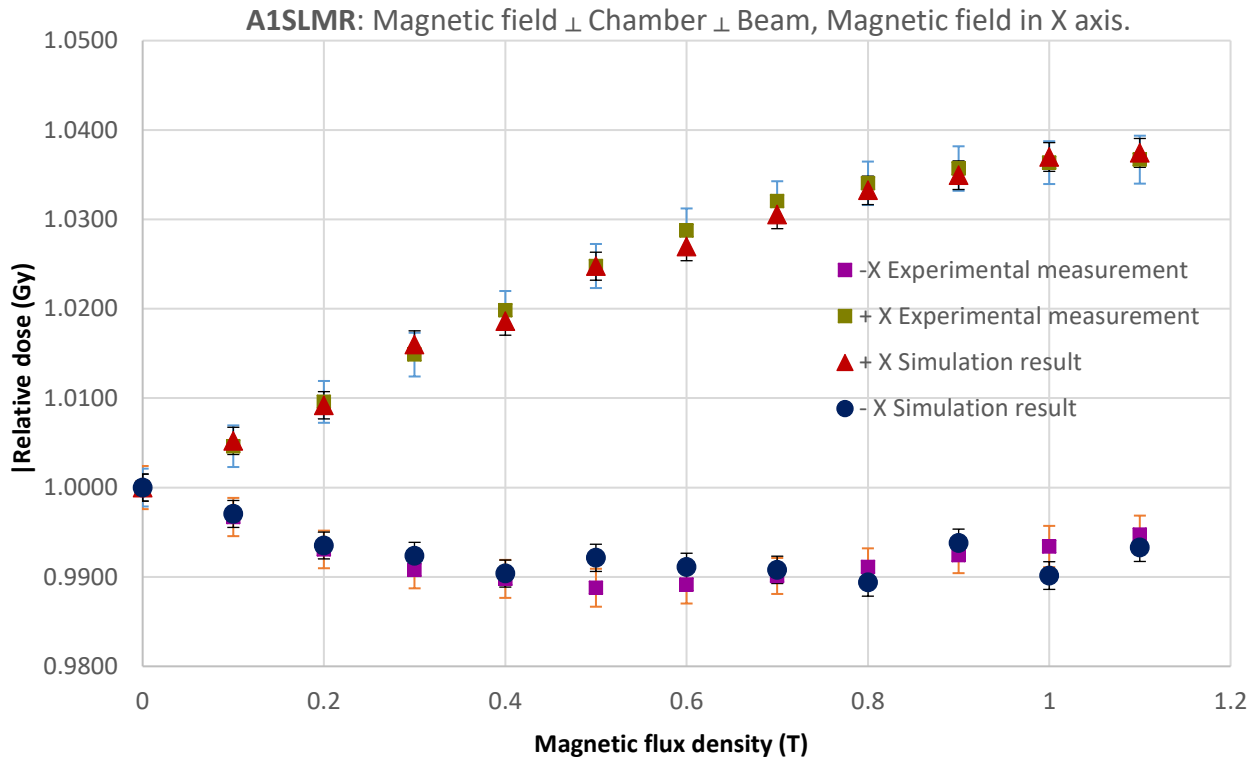

Figure 33. A1SLMR ionization chamber (Orientation I); the experimental and simulation measurements in X direction. The error bars on each data show the relative uncertainty.

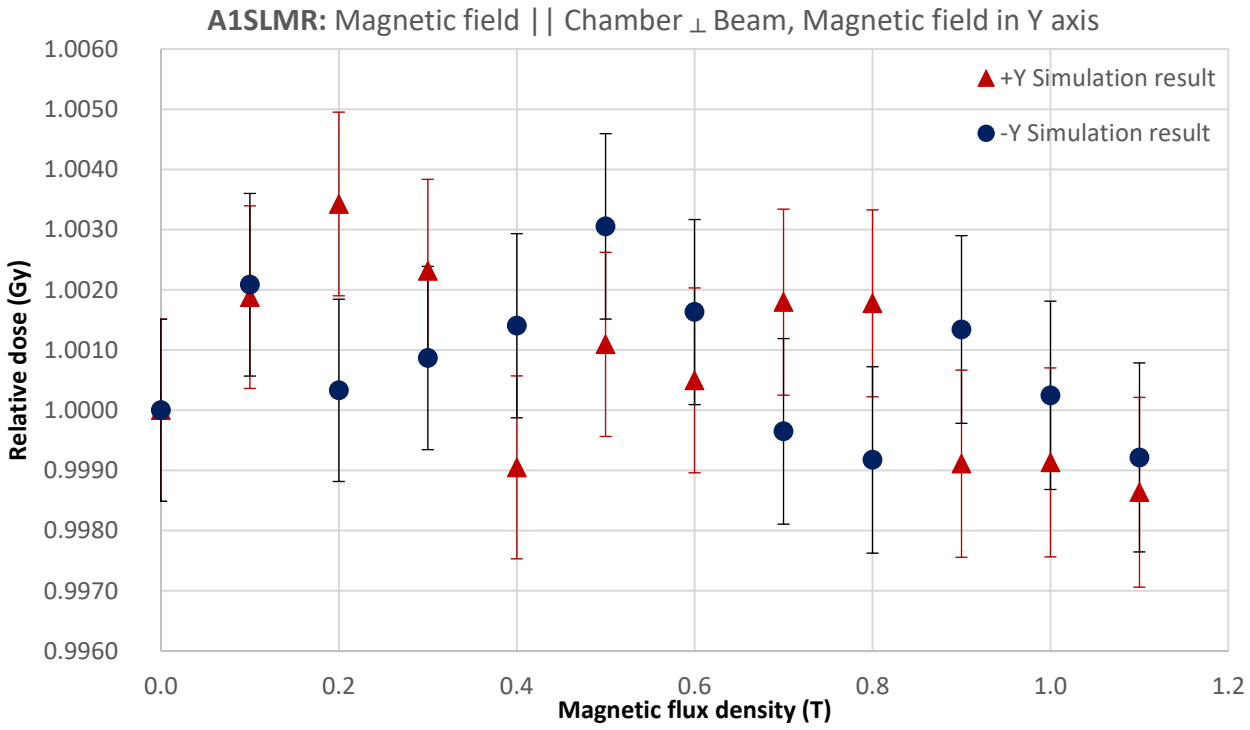

Figure 34. A1SLMR ionization chamber (Orientation II); the simulation measurements in Y direction. The error bars on each data show the relative uncertainty.

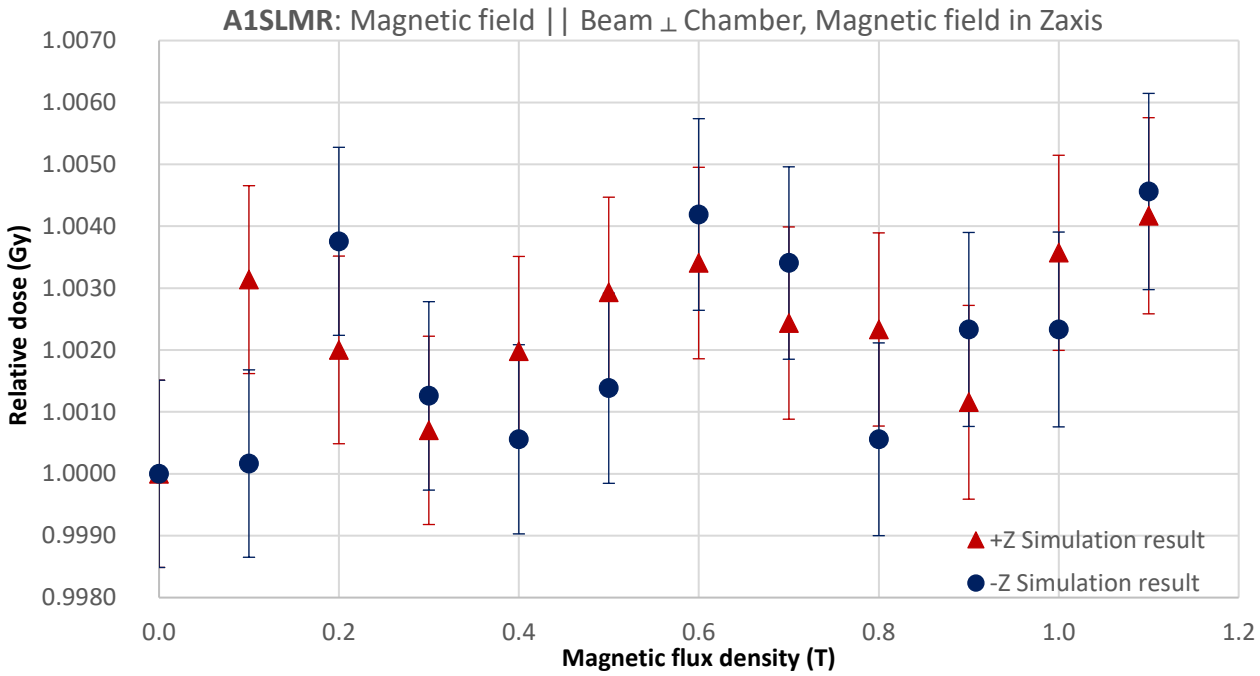

Figure 35. A1SLMR ionization chamber (Orientation III); the simulation measurements in Z direction. The error bars on each data show the relative uncertainty.

A1SLMR ionization chamber

The plot in orientation I shows a good agreement of simulation and measurement results. The response gradually increases with the magnetic flux density to 1.037 at 1.1 T. But by reversing the polarity, the response shows the opposite trend. The response decreases with the magnetic flux density down to 0.988 at 0.5 T, then increases towards 1.0 with increasing magnetic flux density. The statistical uncertainty of the simulations remains below 0.16%.

For orientation II, the simulation shows no appreciable change in response with the magnetic flux density; the response varies between 1.003 and 0.999 for both the polarities. In this orientation, the chamber response shows small change to magnetic flux density, the response varies within ±0.3%. The statistical uncertainty of the simulation remains below 0.15%.

For orientation III, the longitudinal configuration shows unpredictable response to the magnetic flux density, varying between 1.005 and 1.00 for both polarities.

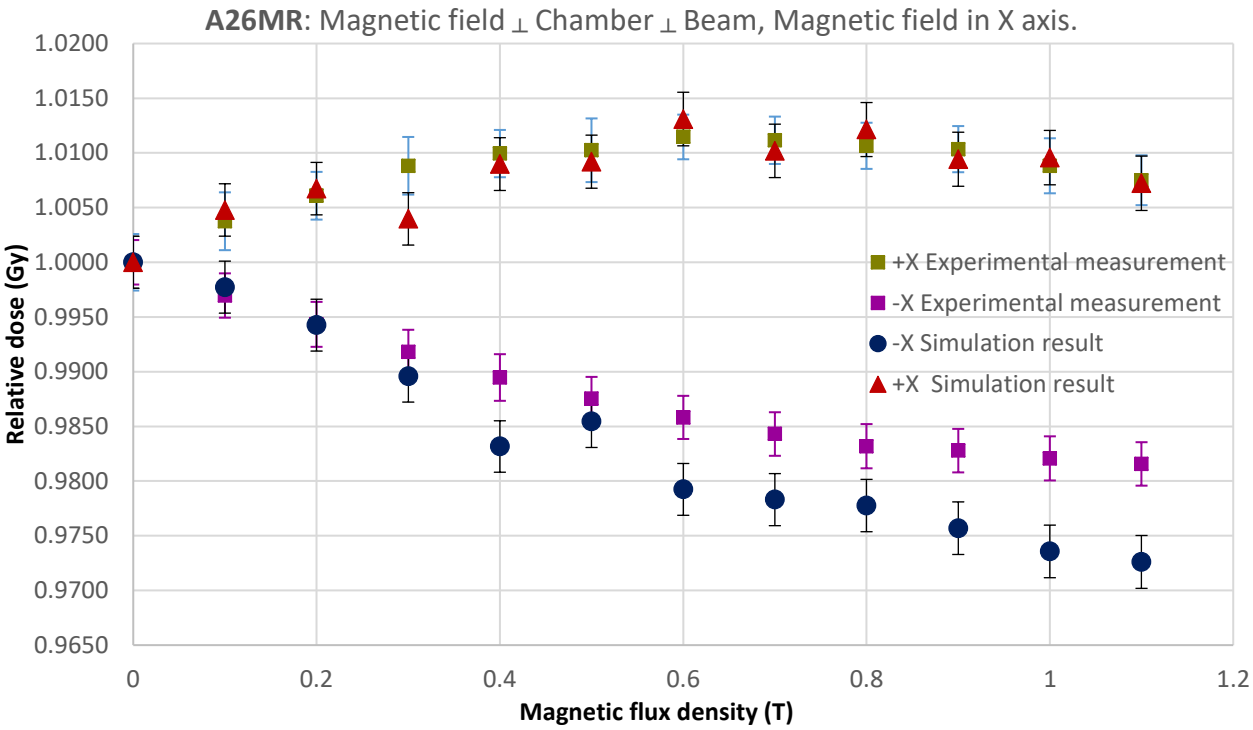

Figure 36. A26MR ionization chamber (Orientation I); the experimental and simulation measurements in X direction. The error bars on each data show the relative uncertainty.

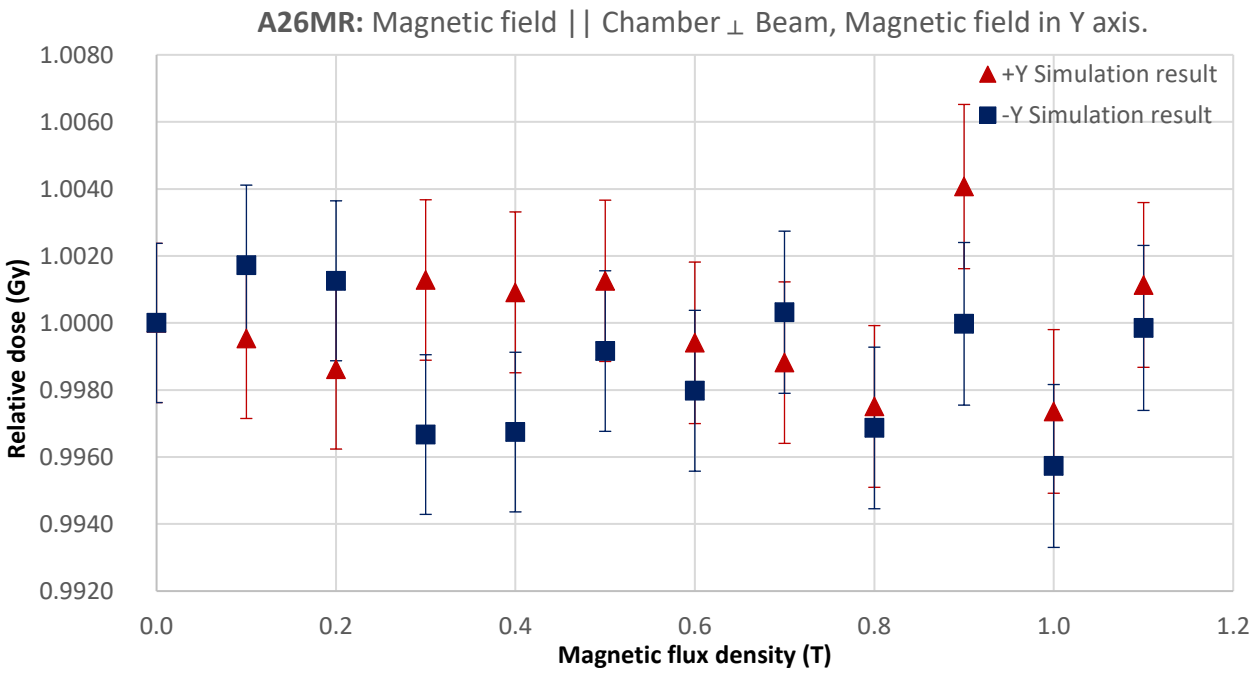

Figure 37. A26MR ionization chamber (Orientation II); the simulation measurements in Y direction. The error bars on each data show the relative uncertainty.

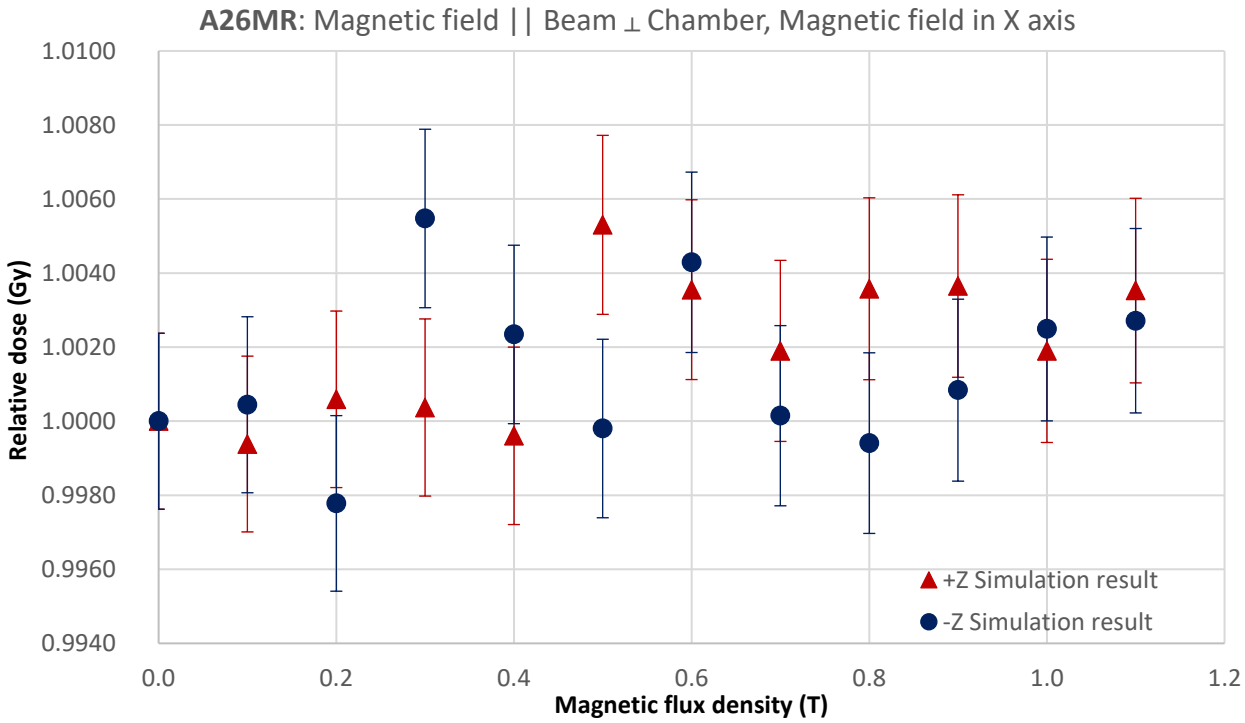

Figure 38. A26MR ionization chamber (Orientation III); the simulation measurements in Z direction. The error bars on each data show the relative uncertainty.

A26MR ionization chamber

The chamber with very small cavity volume exhibited major differences in response for minor changes in the geometry. The simulation results with the chamber modelled according to the technical specifications did not match the result of the experimental measurements. With the help of the micro-CT images, air was added in the stem. As a consequence, the measured results were better approximated by the simulations. The simulation and measurement results show a good agreement: the response increases gradually with magnetic flux density up to 1.031 at 0.5 T and then slightly decreases with increasing magnetic flux density. By reversing the polarity, the simulation and measurement results do not show a good agreement. The response decreases with the magnetic flux density for both the results, to 0.97 in the simulation and to 0.981 in the experimental measurement. The statistical uncertainty of the simulation remains below 0.25%.

For orientation II, the simulation and measurement results show no appreciable relation to the magnetic flux density, varying between 1.004 and 0.996 for both polarities. The statistical uncertainty of the simulation remains below 0.24%.

In the longitudinal configuration, orientation III, an unpredictable response to the magnetic flux density is observed, varying between 1.006 and 0.998 for both polarities.

The orientation I (transverse), magnetic perpendicular to the beam and chamber axis, shows a considerable change in chamber response for all chambers investigated. A plausible explanation was given in (Meijsing, 2009): The lateral surface is small compared to the anterior surface of the ionization chamber. The electrons are deflected towards the lateral side of the ionization chamber, resulting in an overall decrease of electrons entering the cavity as a function of the magnetic flux density. In the same way, the electron path length increases in the beginning, as the electrons get influenced by the Lorentz force and the electron trajectories are bent towards the longitudinal axis of the ion chamber. Depending on the energy of the electrons for a certain magnetic flux density, the path length will start to decrease, as described in **Figure 40.** Also, as described in section 2.4.3, the path length of the electrons in the cavity changes the amount of created charge with magnetic field compared with no magnetic field.

The results of orientation I for the A19MR Farmer-type ionization chamber shown in **Figure 26**, where the chamber response gradually increases approximately by 8.4% up to 0.9 T and slowly decreases with higher magnetic flux densities, which shows a good agreement with the measurement and simulation results performed for the Farmer-type chamber NE2571 by (Meijsing, 2009) and shown in **Figure 39**, where it increases approximately by 8.3% at 1 T. For a magnetic flux density above 1 T, the response of the chamber decreases, since the trajectory length of the electrons in the chamber cavity varies with the strength of the magnetic field.

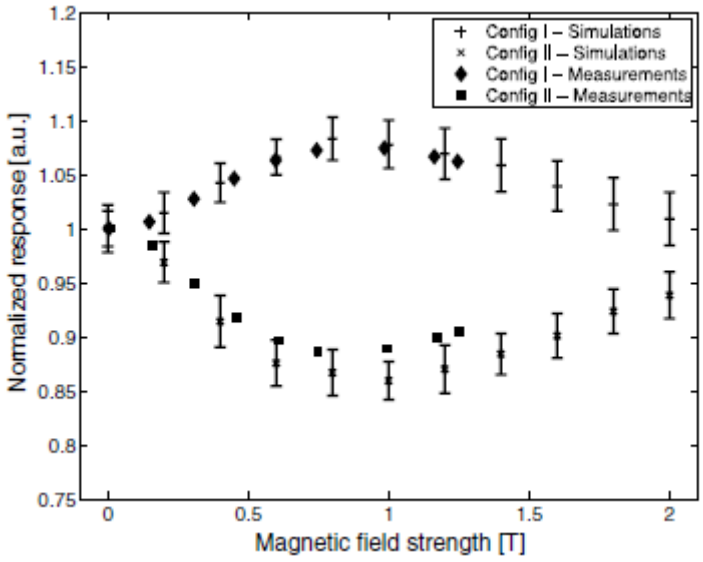

Figure 39. Geant4 simulations and measurements of the Farmer-type chamber NE2571. Configuration I: Magnetic field perpendicular to the ion chamber and photon beam axis, applicable for this thesis (corresponds to orientation I). (Meijsing, 2009)

The orientation I simulation results are in good agreement with the experimental measurements for all the three chambers, except the A26MR chamber. For this chamber, the simulated chamber response differs about 1% from the measured response for a magnetic flux density of 0.6 T in

negative direction, where the simulation results are lower than the experimental measurements. This is most likely due to small details in the chamber model, namely small air regions in the stem of the ion chamber. The response of the A26MR ion chamber turned out to be very sensitive to small changes in the simulation chamber model, which can be associated with its extremely small (micropoint, 0.05 cm^3) sensitive volume.

By reversing the magnetic pole shoe polarity, the response of the A19MR chamber remains below the response for the other polarity and it shows the opposite trend for the hemispherical top chambers A1SLMR and A26MR. A plausible explanation could be associated with the number of electrons entering the cavity, which is lower in reverse polarity.

The maximum dose response was 1.084, 1.037 and 1.012 for the chambers A19MR, A1SLMR and A26MR, respectively. This can be related to the sensitive volume of the ionization chamber, as the path length of secondary electrons in cavity gets larger in magnetic fields as a result of its circular pathway. **Figure 40** illustrates the initial increase of average path length, as the electron trajectories are bent in the direction of longitudinal axis of the ionization chamber. Analogously to **Figure 40**, it can be said that, for a given magnetic flux density the mean electron track length in a chamber with large volume is adequately large and is smaller for smaller chambers, as the electrons have only space to be bent not to be turned.

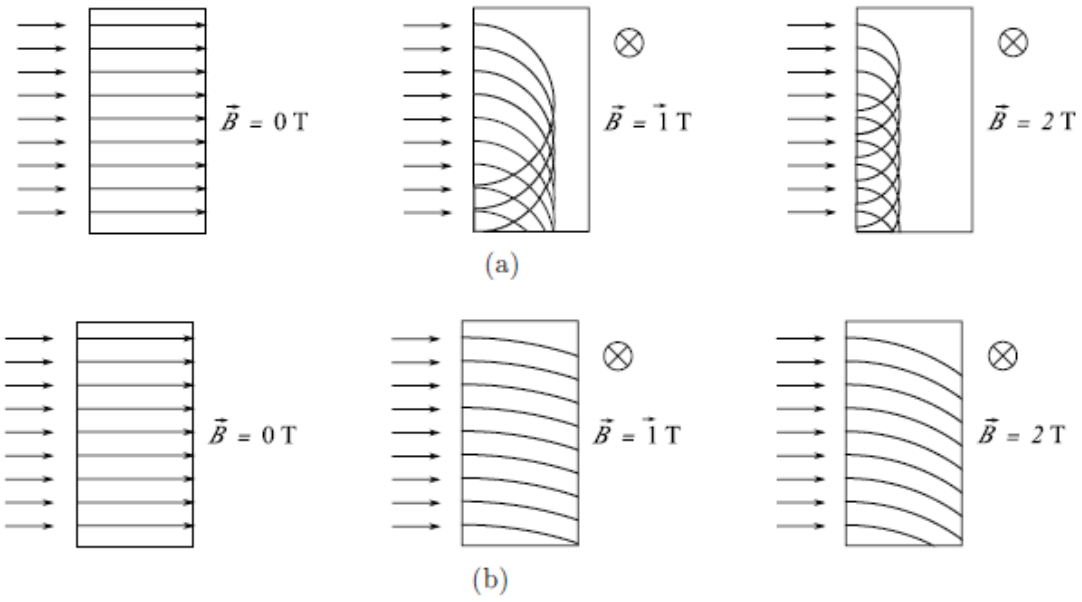

Figure 40. Schematic drawing of electron tracks depending on its own energy and the magnetic flux density for Configuration I. (a) for 1 MeV and (b) for 6 MeV. (Meijsing, 2009)

For orientation II (magnetic field perpendicular to beam, parallel to the chamber) and orientation III (magnetic field parallel to the beam and perpendicular to chamber), only small change in

response with increasing magnetic flux density can be observed. There is less than 0.5% change in response up to the magnetic flux density of 1.1 T for both orientations.

In orientation III, the electrons are focused along the magnetic field lines due to the Lorentz force. The simulation results agree with the results previously published by (Reynolds, et al., 2015). Simulation results for all the three chambers with and without magnetic fields applied during irradiation are close to 1.0. The simulation of all the three ionization chambers suggest, that there is no appreciable ionization chamber response with respect to magnetic flux density in longitudinal orientation. This small response was expected, as electrons are being driven along the magnetic field lines.

For orientation II, there were no previous data available to study. The response can be related to the number of electrons and their track length within the cavity of the chamber, as previously stated by (Meijsing, 2009). In orientation II, the Lorentz force deflects the electrons along the transverse axis of the ionization chamber.

The future task would be to calculate the magnetic field correction factors for the chambers. The new correction factor that corrects for the effect of the magnetic field on the response of the ionization chamber, $k_B^{Q_{msr}}$ is defined by:

$$k_B^{Q_{msr}} = \frac{D_{w,Q_{msr}}^{B} / M_{Q_{msr}}^{B}}{D_{w,Q_{msr}} / M_{Qmsr}} = \frac{D_{w,Q_{msr}}^{B,f_{msr}} / D_{ch,Q_{msr}}^{B}}{D_{w,Q_{msr}} / D_{ch,Q_{msr}}} \tag{10}$$

Here, *msr* stands for machine-specific reference field, Q_{msr} indicates that this factor also depends on beam quality as the gyroradius of electrons depends on their kinetic energy, $D_{w,Q_{msr}}^{f_{msr}}$ is absorbed dose to water for field f_{msr} with beam quality Q_{msr} . M_Q^B is the corrected chamber reading, $D_{w,Q_{msr}}^{B,f_{msr}}$ is the absorbed dose to water in the magnetic field *B* for field f_{msr}. $D_{ch,Qmsr}$ is the dose deposited in the sensitive volume of the ion chamber in presence and absence of the magnetic field, respectively. The equation is valid for the assumption that the mean energy deposited in air per Coulomb of charge released, does not depend on the magnetic flux density (O'Brien, et al., 2016).

5. Conclusions

1. In this project, an experimental setup according to the IAEA TRS-398 dosimetry protocol and Monte Carlo simulations were used to investigate the response of ion chambers in magnetic fields.
2. The Monte-Carlo simulations using EGSnrc for the three recently developed MR-compatible chambers have been validated by measurements for three orientations of chamber with respect to the photon beam and the magnetic field. Three geometrically different ionization chambers were modelled and simulated, namely A19MR Farmer-type ionization chamber, A1SLMR slimline miniature ionization chamber and A26MR micro ionization chamber.
3. It was found, that the ionization chamber response increases up to 8.4% at 0.9 T in orientation I (transverse); the magnetic field perpendicular to the beam and chamber axis; and was similar as investigated by (Meijsing, 2009). For the orientation III (longitudinal); the magnetic field parallel to the beam axis, no discernable change in response as a function of the magnetic field is found. The ionization chamber response is in near vicinity of previously simulated results by (Reynolds, et al., 2015). It was found, that the chamber response shows no appreciable change to the magnetic flux density in orientation II; the magnetic field parallel to the chamber axis. And there were no previous data available for orientation II to study the result.
4. It was observed, that the cavity size of the ionization chamber affects the chamber response in presence of a magnetic field. It was found, that the dose response increases up to 8.4%, 3.7% and 1.2% for cavity sizes of 0.62 cm^3, 0.053 cm^3 and 0.015 cm^3, respectively.

The response of the ionization chambers as a function of the magnetic field is understood and was successfully simulated using the EGSnrc Monte-Carlo code.

6. Acknowledgements

I would like to express my gratitude to **Professor Oliver Jäkel** for giving me the opportunity to write my thesis in the department of Medical Physics in Radiation Oncology at German Cancer Research Center (Deutsches Krebsforschungszentrum, DKFZ, Heidelberg, Germany).

I would also like to acknowledge **Professor Diana Adliene** at Kaunas University of Technology (Kaunas, Lithuania) for her support throughout my Master's study. I am grateful to have her as my mentor and professor during my course of Medical Physics study. Sincere thanks for her comments on this thesis.

Furthermore, I would like to express heartfelt thanks to **Dr. Asja Pfaffenberger** at DKFZ for introducing me to the topic, as well as for the unconditional motivation along the way. The door to her office was always open whenever I needed advice or a solution to a query about my research or writing. And her constant guidance helped me drive my passion in the right direction and expanding my knowledge.

Moreover, I would like to express my sincere gratitude to my advisor **Claudia Katharina Spindeldreier** at DKFZ for her continuous support, kind nature, motivation and especially, for her patience throughout the thesis work. Her guidance helped me during the time of research and enormously with writing of this thesis. I could not have imagined having a better advisor and mentor for my thesis.

I would also like to thank Dr. Peter Häring, Clemens Lang and Mona Splinter for facilitating the linac measurements, and Armin Runz for designing the chamber holders. I am grateful to Professor Dr. Markus Alber from Heidelberg University Hospital for supporting this project and to Standard Imaging Inc. for providing the chamber details that were required for accurate modelling of the chambers for simulation. I appreciate the help from the core facility small animal imaging, for providing micro-CT data of the ionization chamber. I would also like to thank the group of Medical Physics in Radiation Oncology Department at DKFZ, for their cooperation and of course friendship.

I would also like to thank my **friends** and **family** for their moral support. And special thanks to Dhwalin Shukla for prompt help with computer troubleshoot.

Finally, I would like to express my very profound gratitude to my parents, **Kaku** and **Sapna** for providing me with never-ending support and continuous encouragement throughout my years of study and through the process of researching and writing this thesis. This accomplishment would not have been possible without them.

Thank you.

7. References

Alberta Health Services. *LINAC-MR Cross Cancer Institute.* 2016. [Online]
Available at: http://www.mp.med.ualberta.ca/linac-mr/details.html
[Accessed 15 05 2017].

BAKENECKER, A. C. Dose measurements with ionization chambers in magnetic fields using 6MeV photons. 2014. In: *Master thesis.* Heidelberg: s.n.

BASKAR, R. et al. Biological response of cancer cells to radiation treatment. *Front Mol Biosci,* 2014, 1, 24.

BILLE, J and SCHLEGEL, W. Medizinische Physik 2. In: Springer, ed. *Medizinische Strahlenphysik.* s.l.:s.n.

BUCCIOLINI, M. et al. Diamond detector versus silicon diode and ion chamber in photon beams of diffrernt energy and field size. *Med Phys*, 2003, 30(8), 2149-2154.

CRIJNIS, S. & RAAYMAKERS, B. From static to dynamic 1.5T MRI-linac prototype: impact of gantry position related magnetic field variation on image fidelity. *Physics in Medicine and Biology,* 2014, 59, 13.

DEMPSEY, J. et al. A Real-Time MRI Guided External Beam Radiotherapy Delivery System.. *Medical Physics,* 2006, 33(6), 2254.

DRZEZO. *Radiology Key.* 2016. [Online]
Available at: https://radiologykey.com/dose-distribution-and-scatter-analysis-2/
[Accessed 15 05 2017].

FADDEGON, B. et al. Accuracy of EGSnrc, Geant4 and PENELOPE Monte Carlo systems for siulation of electron scatter in external beam radiotherapy. *Phys. Med. Biol.,* 2009, 54(20), 6151-6163.

FALLONE, B. et al. First MR images obtained during megavoltage photon irradiation from a prototype integrated linac-MR system. *Med. Phys., 2009,* 36, 2084{2088}.

FEDOROV, A. et al. 3D Slicer as an Image Computing Platform for the Quantitative Imaging Network.. *Magn Reson Imaging,* 2012, 30(9), 1323-41.

GODDU, S., PECHENAYA GREEN, O. & MUTIC, S. TG-51 calibration of first commercial MRI-guided IMRT system in the presence of 0.35 T magnetic field.. *Med Phys*, 2012, 39, 3968.

GUPTA, T. & NARAYAN, C. A. Image-guided radiation therapy: Physician's perspectives. *J Med Phys,* 2012, 37(4), 174-82.

IAEA. International Atomic Energy Agency IAEA. Absorbed dose determination in external beam radiotherapy: an international code of practice for dosimetry based on standards of absorbed dose to water. 2000. In: *Technical Report Series 398 (TRS 398).* s.l.:s.n.

ICRU report 50. *Prescribing, Recording and Reporting Photon Beam Therapy,* 1993. s.l.: s.n.

ICRU report 62. *Supplement to ICRU Report no. 50,* 1999. s.l.: s.n.

JAFFRAY, D., CARLONE, M. & MILOSEVIC, M. A facility for magnetic resonance-guided radiation therapy. *Semin. Radiat. Oncol.,* 2014, 24.

JAN J W LAGENDIJK, BAS W RAAYMAKERS, CORNELIS A T VAN DEN BERG, MARINUS A MOERLAND, MARIELLE E PHILIPPENS AND MARCO VAN VULPEN. 2014. *IOPscience.* [Online]
Available at: http://iopscience.iop.org/article/10.1088/0031-9155/59/21/R349

KARLSSON, M. et al. Dedicated magnetic resonance imaging in the radiotherapy clinic.. *Int. J. Radiat. Oncol. Biol. Phys.,* 2009, 74, p. 644{651}.

Kawrakow, I. *EGSnrc C++ class library,* 2006. s.l.: NRC report PIRS:898.

KAWRAKOW, I. & ROGERS, D. The EGSnrc code system: Monte Carlo simulation of electron and photon transport. 2000. In: s.l.:s.n.

KEALL, P. J., BARTON, M., FRANZCR & CROZIER, S. The Australian Magnetic Resonance Imaging–Linac Program. *Radiation oncology,* 2014, 24(3), 203-206.

KHAN, F. M., SEWCHAND, W., LEE, J. et al. Revision of tissue- maximum ratio and scatter-maximum ratio concepts for cobalt-60 and higher energy x-ray beams.. *Med Phys,* 1980, 7, 230.

KIRKBY, C., MURRAY, B., RATHEE, S. & FALLONE, B. Lung dosimetry in a linac-MRI radiotherapy unit with a longitudinal magnetic field.. *Med. Phys.,* 2010, 4722-32.

KITAMURA, K., SHIRATO, H. & SEPPENWOOLDE, Y. Tumor location, cirrhosis, and surgical history contribute to tumor movement in the liver, as measured during stereotactic irradiation using a real-time tumor-tracking radiotherapy system. *Int. J. Radiat. Oncol. Biol. Phys.,* 2003, 56, 221{228}.

LAGENDIJK, J. et al. MR Guidance in Radiotherapy. *Phys Med Biol,* 2014, 59(21) (10.1088/0031-9155/59/21/R349), R349-69.

LAGENDIJK, J. et al. MRI/linac integration. *Radiotherapy oncology,* 2008, 86, 25-9.

MagnetTx Oncology Solutions, i., 2016. *magnettx.com.* [Online]
Available at: http://www.magnettx.com/index.php/author/root/

MALKOV, V. N. & ROGERS, D. W. O. Charged particle transport in magnetic fields in EGSnrc. *Medical Physics,* 2016, 43, 4447–4458.

MEIJSING, et al. Dosimetry for the MRI accelerator: the impact of a magnetic field on the response of Farmer NE2571 ionization chamber. *Phys. Med. Biol,* 2009, 54, 2993-3002.

Messelektronik Schwarzbeck, n.d. *Electromagnet with variable Air Gap AGEM.* s.l. Patent No. 5520.

MOHAN, R., CHUI , C. & LIDOFSKY, L. Energy and angular distributions of photons from medical linear accelerators. *Med. Phys.,* 1985, 12, 592.

MUTIC, S., JAMES, F. & DEMPSEY. The ViewRay System: Magnetic Resonance–Guided and Controlled Radiotherapy. *Seminars in Radiation Oncology,* 2014, 24(3), 196-199.

OBORN, B. *Modelling and Concepts in MRI-guided Photon and Proton Beam therapy.* Australia(Wollongong, NSW 2522, Wollongong Hospital, NSW 2500), 2016.: s.n.

OBORN, B., METCALFE, P., BUTSON, M. & ROSENFELD, A. Monte Carlo characterization of skin doses in 6 MV transverse orientation, magnetic field strength and exit bolus.. *Med. Phys.,* 2010, 37, 5208-17.

OBORN, B. et al. Electron contamination modeling and skin dose in 6 MV longitudinal MRI fringe field.. *Med. Phys.,* 2012, 39, 874-90.

O'BRIEN, D. J., ROBERTS, D. A., IBBOTT, G. S. & SAWAKUCHI, G. O. Reference dosimetry in magnetic fields: formalism and ionization chamber correction factor. *Med Phys,* 2016, 43, 4915.

O'NEILL, M., LAM, W., PARTOWMAH, M. & KHALIFEH, A. External beam profile measured with film or ionization chamber.. *Med. Dosim.,* 1988, 13, 167-9.

RAAIJMAKERS, A., RAAYMAKERS, B. & LAGENDIJK, J. Experimental verification of magnetic field dose effects for the MRI-accelerator.. *Phys. Med. Biol.,* 2007, 14, 4283.

RAAIJMAKERS, A., RAAYMAKERS, B. & LAGENDIJK, J. Magnetic-field-induced dose effects in MR-guided radiotherapy systems: dependence on the magnetic field strength.. *Phys.Med. Biol.,* 2007, 4, 909.

RAAIJMAKERS, A., RAAYMAKERS, B., VAN DER MEER, S. & LAGENDIJK, J. Integrating a MRI scanner with a 6MV radiotherapy accelerator: impact of the surface orientation on the entrance and exit dose due to the transverse magnetic field. *Phys. Med. Biol.,* 2007, 4, p. 929.

RAAYMAKERS B W et al. Integrating a 1.5 T MRI scanner with a 6 MV accelerator: proof of concept. *Phys. Med. Biol,* 2009, 54, N229-37.

RAAYMAKERS, B. et al. Integrating a MRI scanner with a 6 MV radiotherapy accelerator: dose deposition in a transverse. *Phys. Med. Biol.,* 2004, 4109-4118.

RAAYMAKERS, B., RAAIJMAKERS, A. & LAGENDIJK, J. Integrating a MRI scanner with a 6 MV radiotherapy accelerator: dose increase at tissue–air interfaces in a lateral magnetic field due to returning electrons. *Phys. Med. Biol,* 2005, 50, 1363-76.

RAAYMAKERS, B. et al. Dosimetry in strong magnetic fields; issues and opportunities.. *Radiother. Oncol.,* 2012, 103, S170.

Radblog. *RAD-Planning.* 2013. [Online]
Available at: http://rad-planning.com/RADblog/2012/10/16/image-guided-radiation-therapy/

REYNOLDS, M., FALLONE, B. G. & RATHEE, S. Dose response of selected ion chambers in applied homogeneous transverse and longitudinal magnetic fields. *Med. Phys.,* 2013, Volume 40, 42102.

REYNOLDS, M., FALLONE, B. G. & RATHEE, S. Technical Note: Response measurement for select radiation detectors in magnetic fields. *Medical Physics,* 2015, 42(6), 2837-2840.

REYNOLDS, M., FALLONE, B. & RATHEE, S. Dose response of selected solid state detectors in applied homogeneous transverse and longitudinal magnetic. *Med. Phys.,* 2014, 41, 092103.

ROBERT, N. & CHERRY, J. *Encyclopedia of occupational health and safety.* 2011, [Online] Available at: http://www.iloencyclopaedia.org/contents/part-vi-16255/radiation-ionizing [Accessed May 2017].

ROGERS, D. Fifty years of Monte Carlo simulations for Medical Physics. *Phys Med Biol,* 2006, 35(4), R287-R301.

ROGERS, D., WALTERS, B. & KAWRAKOW. The EGSnrc Users Manual. 2007 In: s.l.:s.n.

RUSTGI, S. N. & FRYE, D. M. D. Dosimetric characterization of radio-surgical beams with diamond detectors.. *Med. Phys.,* 1995, 22(12), 2117-2121.

SAHA & GOPAL, B. *Physics and Radiobiology of Nuclear Medicine.*2006. s.l.:Springer.

SCHLEGEL, W. & BILLE, J. *Medizinische Strahlenphysik*, 2002. s.l.: Springer.

SECO, J. & VERHAEGWN, F. *Monte Carlo Techniques in Radiation Therapy.* 2016. s.l.:CRC Press.

SHELLOCK, F. Reference Manual for Magnetic Resonance Safety Implants and Device. *Biomedical Research Publishing Group.2010.*

SMIT, K. et al. Reference dosimetry for an MRI-Linac in the magnetic field. *Med Phys, 2012,* 39(6), 4010-4011.

SMIT, K. et al. Towards reference dosimetry for the MR-linac: magnetic field correction of the ionization chamber reading. *Phys Med Biol,* 2013, 58(17), 1029.

SMIT, K. et al. Relative dosimetry in a 1.5 t magnetic field: An MRI-linac compatible prototype scanning water phantom.. *Med Phys Biol,* 2014, 59(15), 4099-4109.

SPINDELDREIER, C. K. et al. Dosimetry with Farmer ionization chambers in magnetic fields: influence of the sensitive volume. *ESTRO,* 2017, PO-0761.

Sprawls, P., n.d. *Sprawls education foundation.* [Online]
Available at: http://www.sprawls.org/ppmi2/INTERACT/
[Accessed 26 05 2017].

StandardImaging. *Standardimaging.* 2016. [Online]
Available at: https://www.standardimaging.com/news/article/news-exradin-mr-compatible-ion-chambers-now-available
[Accessed May 2017].

StandardImaging. *www.standardimaging.com.* 2016. [Online]
Available at: https://www.standardimaging.com/exradin/thimble-ion-chambers
[Accessed April 2017].

STARK, R., DEMPSY, J. & LOW, D. Adaptive Motion Compensation in Radiotherapy. *Imaging in Medical Diagnosis and Therapy,* 2011, 115{128}.

tesec-int.org, n.d. *tesec.* [Online]
Available at: http://www.tesec-int.org/TechHaz-site%2008/Radiation-interaction.pdf
[Accessed May 2017].

THARIAT, J. *Nat. Rev. Clin. Oncol.*, 2013, Issue 10, 52-60.

University of Alberta & Cross Cancer institute, 2013. [Online]
Available at: http://www.mp.med.ualberta.ca/linac-mr/photo_gallery.html#phase-2

VAN SOERNSEN DE KOSTE, J. et al. Renal mobility during uncoached quiet respiration: An analysis of 4DCT scans. *Int. J. Radiat. Oncol. Biol. Phys.*, 2006, 64, 799{803}.

Wikimedia Commans. *Nuclear Power.* 2017 [Online]
Available at: http://www.nuclear-power.net/nuclear-power/reactor-physics/interaction-radiation-matter/interaction-gamma-radiation-matter/#prettyPhoto
[Accessed 15 05 2017].

WOLTHAUS, J. et al. Comparison of different strategies to use four-dimensional computed tomography in treatment planning for lung cancer patients.. *Int. J. Radiat. Oncol. Biol. Phys.*, 2008, 70 (10.1016/j.ijrobp.2007.11.042.), 1229{1238}.

WULFF, J., ZINK, K. & KAWRAKOW, I. Efficiency improvements for ion chamber calculations in high energy. *Med. Phys.*, 2008, 35(4), 1328-1336.

YAN, D., VICINI, F., WONG, J. & MARTINEZ, A. Adaptive Radiation Therapy. *Phys Med Biol,* 1997, 42(1), 123-32.

8. Appendices

8.1 Beam spectrum used for simulation

Mohan et al 6 MV spectrum: cts/bin or /MeV

Energy (MeV)	Counts (cts/bin)		
0.25	0.0041078	3.25	0.1484442
0.50	0.1295177	3.50	0.09496227
0.75	0.4609022	3.75	0.1246583
1.00	0.4609022	4.00	0.09773248
1.25	0.4435880	4.50	0.05154921
1.50	0.4084962	4.75	0.04184013
1.75	0.4084962	5.00	0.04803306
2.00	0.2496504	5.25	0.01624749
2.25	0.2367691	5.50	0.02715377
2.50	0.1867142	5.75	0.01199324
2.75	0.1382681	6.00	0.01573713
3.00	0.1304545		

The spectrum was taken from:

https://github.com/nrc-cnrc/EGSnrc/blob/master/HEN_HOUSE/spectra/mohan6.spectrum

8.2 Simulation results

A19MR ionization chamber

```
            ***********************************************
            *                                             *
            *               egs_chamber CSE)              *
            *                                             *
            ***********************************************

This is EGS_ChamberApplication Revision: 1.15  based on
EGS_AdvancedApplication Revision: 1.39



======================== geometry ====================
type = EGS_EnvelopeGeometry
name = CHAMBER_IP_R3
number of regions = 93
base geometry = phantom (type EGS_XYZGeometry)
inscribed geometries:
   CHAMBER_0_R3 (type EGS_EnvelopeGeometry)
=======================================================


The simulation uses the following source:
=========================================
 Collimated source from a shape of type point onto a shape of type rectangle with
tabulated            histogram            spectrum            defined            in
/usr/local/sw/modules/source/EGSnrc/HEN_HOUSE/spectra/mohan6.spectrum, photons


Random number generator:
========================================
type                 = ranmar
high resolution      = no
initial seeds        = 33 102
numbers used so far = 5617508352




The following media are defined:
================================

0  C552521ICRU              AE= 0.5210 AP= 0.0100 0
1  H2O521ICRU               AE= 0.5210 AP= 0.0100 1
2  AIR521ICRU               AE= 0.5210 AP= 0.0100 2

3  CU521ICRU                AE= 0.5210 AP= 0.0100 3
4  TEFLON521ICRU            AE= 0.5210 AP= 0.0100 4
5  AL521ICRU                AE= 0.5210 AP= 0.0100 5


Transport parameter and cross section options:
==============================================
Photon cross sections                           xcom
```

```
Compton cross sections                          default
Global Pcut                                     0.01
Pair cross sections                             BH
Pair angular sampling                           Simple
Triplet production                              Off
Bound Compton scattering                        norej
Radiative Compton corrections                   Off
Rayleigh scattering                             Off
Atomic relaxations                              On
Photoelectron angular sampling                  On
Photonuclear attenuation                        Off
Photonuclear cross sections                     default

Global Ecut                                     0.521
Brems cross sections                            BH
Brems angular sampling                          KM
Spin effects                                    Off
Electron Impact Ionization                      Off
Global Smax                                     1e+10
ESTEPE                                          0.1
Ximax                                           0.1
Boundary crossing algorithm                     Exact
Skin depth for BCA                              3
Electron-step algorithm                         EGSnrc
================================================

Variance reduction
==================================================
Photon splitting = off
Range rejection = Russian Roullette (RR)
rejection in cavity for E < 0.521
else RR with survival probability 0.015625
rejection geometry is CHAMBER_IP_R3


photon cross-section enhancement = On
 1) CHAMBER_IP_R3
    regions    :  1 2 3 4 5 6 7 8 9 10 11 12 13 14 15 16 17 18 19 20 21 22 23 24
25 26 27 28 29 30 31 32 33 34 35 36 37 38 39 40 41 42 43 44 45 46 47 48 49 50 51
52 53 54 55 56 57 58 59 60 61 62 63 64 65 66 67 68 69 70 71 72 73 74 75 76 77 78
79 80 81 82 83 84 85 86 87 88 89 90 91 92
    enhancement:  64 64 64 64 64 64 64 64 64 64 64 64 64 64 64 64 64 64 64 64 64
64 64 64 64 64 64 64 64 64 64 64 64 64 64 64 64 64 64 64 64 64 64 64 64 64 64 64
64 64 64 64 64 64 64 64 64 64 64 64 64 64 64 64 64 64 64 64 64 64 64 64 64 64 64
64 64 64 64 64 64 64 64 64 64 64 64 64 64 64 64 64 64 64 64 64 64 64 64 64 64 64


region by region ECUT = Off

==========================================

Suming the following .egsdat files:
=====================================================================
 1 00a19_w1.egsdat               ncase=5333300       cpu=527.34
 2 00a19_w2.egsdat               ncase=5333350       cpu=489.26
 3 00a19_w3.egsdat               ncase=5866630       cpu=522.82
 4 00a19_w4.egsdat               ncase=5333300       cpu=510.44
 5 00a19_w5.egsdat               ncase=5333300       cpu=508.77
```

```
 6 00a19_w6.egsdat                ncase=5333300        cpu=526.91
 7 00a19_w7.egsdat                ncase=5333300        cpu=518.10
 8 00a19_w8.egsdat                ncase=5866630        cpu=497.04
 9 00a19_w9.egsdat                ncase=4799970        cpu=504.46
10 00a19_w10.egsdat               ncase=5333300        cpu=486.27
11 00a19_w11.egsdat               ncase=5333300        cpu=510.97
12 00a19_w12.egsdat               ncase=5333300        cpu=495.10
13 00a19_w13.egsdat               ncase=5333300        cpu=498.21
14 00a19_w14.egsdat               ncase=5333300        cpu=453.93
15 00a19_w15.egsdat               ncase=4799970        cpu=481.96
=============================================================================
                            Total ncase=79999550       cpu=7531.58


Finished simulation

Total cpu time for this run:            0.01 (sec.) 0.0000(hours)
CPU time including previous runs:       7531.59 (sec.) 2.0921(hours)
Histories per hour:                     3.82387e+07
Number of random numbers used:          84070204692
Number of electron CH steps:            4.76891e+09
Number of all electron steps:           6.52671e+09


last case = 79999550 fluence = 7999.95

Geometry                        Cavity dose
------------------------------------------------
Geometry Type: EGS_EnvelopeGeometry     CHAMBER_IP_R3             4.1016e-12 +/-
0.133  %



End of run                                              Thu Mar 30 13:20:54 2017
=============================================================================
```

A1SLMR ionization chamber

```
               ************************************************
               *                                              *
               *               egs_chamber CSE)               *
               *                                              *
               ************************************************

This is EGS_ChamberApplication Revision: 1.15  based on
EGS_AdvancedApplication Revision: 1.39



======================== geometry ====================
type = EGS_EnvelopeGeometry
name = CHAMBER_IP_R3
number of regions = 322
base geometry = phantom (type EGS_XYZGeometry)
inscribed geometries:
   CHAMBER_0_R3 (type EGS_EnvelopeGeometry)
======================================================


The simulation uses the following source:
=========================================
 Collimated source from a shape of type point onto a shape of type rectangle with
tabulated            histogram            spectrum            defined            in
/usr/local/sw/modules/source/EGSnrc/HEN_HOUSE/spectra/mohan6.spectrum, photons


Random number generator:
========================================
type                = ranmar
high resolution     = no
initial seeds       = 33 97
numbers used so far = 113457158656




The following media are defined:
================================

0  AIR521ICRU               AE= 0.5210 AP= 0.0100 0
1  C552521ICRU              AE= 0.5210 AP= 0.0100 1
2  H2O521ICRU               AE= 0.5210 AP= 0.0100 2
3  CU521ICRU                AE= 0.5210 AP= 0.0100 3
4  TEFLON521ICRU            AE= 0.5210 AP= 0.0100 4
5  POLYCARBONATE521ICRU     AE= 0.5210 AP= 0.0100 5


Transport parameter and cross section options:
==============================================
Photon cross sections                          xcom
Compton cross sections                         default
Global Pcut                                    0.01
Pair cross sections                            BH
```

```
Pair angular sampling                                Simple
Triplet production                                   Off
Bound Compton scattering                             norej
Radiative Compton corrections                        Off
Rayleigh scattering                                  Off
Atomic relaxations                                   On
Photoelectron angular sampling                       On
Photonuclear attenuation                             Off
Photonuclear cross sections                          default

Global Ecut                                          0.521
Brems cross sections                                 BH
Brems angular sampling                               KM
Spin effects                                         Off
Electron Impact Ionization                           Off
Global Smax                                          1e+10
ESTEPE                                               0.1
Ximax                                                0.1
Boundary crossing algorithm                          Exact
Skin depth for BCA                                   3
Electron-step algorithm                              EGSnrc
================================================

Variance reduction
=====================================================
Photon splitting = off
Range rejection = Russian Roullette (RR)
rejection in cavity for E < 0.521
else RR with survival probability 0.015625
rejection geometry is CHAMBER_IP_R3


photon cross-section enhancement = On
 1) CHAMBER_IP_R3
    regions    :  1 2 3 4 5 6 7 8 9 10 11 12 13 14 15 16 17 18 19 20 21 22 23 24
25 26 27 28 29 30 31 32 33 34 35 36 37 38 39 40 41 42 43 44 45 46 47 48 49 50 51
52 53 54 55 56 57 58 59 60 61 62 63 64 65 66 67 68 69 70 71 72 73 74 75 76 77 78
79 80 81 82 83 84 85 86 87 88 89 90 91 92 93 94 95 96 97 98 99 100 101 102 103 104
105 106 107 108 109 110 111 112 113 114 115 116 117 118 119 120 121 122 123 124
125 126 127 128 129 130 131 132 133 134 135 136 137 138 139 140 141 142 143 144
145 146 147 148 149 150 151 152 153 154 155 156 157 158 159 160 161 162 163 164
165 166 167 168 169 170 171 172 173 174 175 176 177 178 179 180 181 182 183 184
185 186 187 188 189 190 191 192 193 194 195 196 197 198 199 200 201 202 203 204
205 206 207 208 209 210 211 212 213 214 215 216 217 218 219 220 221 222 223 224
225 226 227 228 229 230 231 232 233 234 235 236 237 238 239 240 241 242 243 244
245 246 247 248 249 250 251 252 253 254 255 256 257 258 259 260 261 262 263 264
265 266 267 268 269 270 271 272 273 274 275 276 277 278 279 280 281 282 283 284
285 286 287 288 289 290 291 292 293 294 295 296 297 298 299 300 301 302 303 304
305 306 307 308 309 310 311 312 313 314 315 316 317 318 319 320 321
    enhancement:  64 64 64 64 64 64 64 64 64 64 64 64 64 64 64 64 64 64 64 64
64 64 64 64 64 64 64 64 64 64 64 64 64 64 64 64 64 64 64 64 64 64 64 64 64 64
64 64 64 64 64 64 64 64 64 64 64 64 64 64 64 64 64 64 64 64 64 64 64 64 64 64
64 64 64 64 64 64 64 64 64 64 64 64 64 64 64 64 64 64 64 64 64 64 64 64 64 64
64 64 64 64 64 64 64 64 64 64 64 64 64 64 64 64 64 64 64 64 64 64 64 64 64 64
64 64 64 64 64 64 64 64 64 64 64 64 64 64 64 64 64 64 64 64 64 64 64 64 64 64
64 64 64 64 64 64 64 64 64 64 64 64 64 64 64 64 64 64 64 64 64 64 64 64 64 64
64 64 64 64 64 64 64 64 64 64 64 64 64 64 64 64 64 64 64 64 64 64 64 64 64 64
64 64 64 64 64 64 64 64 64 64 64 64 64 64 64 64 64 64 64 64 64 64 64 64 64 64
```

```
64 64 64 64 64 64 64 64 64 64 64 64 64 64 64 64 64 64 64 64 64 64 64 64 64
64 64 64 64 64 64 64 64 64 64 64 64 64 64 64 64 64 64 64 64 64 64 64 64 64
64 64 64 64 64 64 64 64 64 64 64 64 64 64 64 64 64 64 64 64 64 64 64 64 64
64 64 64


region by region ECUT = Off

==========================================

Suming the following .egsdat files:
=========================================================================
 1 00a1sl_w1.egsdat               ncase=160000000      cpu=12238.20
 2 00a1sl_w2.egsdat               ncase=160000000      cpu=11604.70
 3 00a1sl_w3.egsdat               ncase=160000000      cpu=11835.30
 4 00a1sl_w4.egsdat               ncase=160000000      cpu=11565.60
 5 00a1sl_w5.egsdat               ncase=160000000      cpu=11923.10
=========================================================================
                            Total ncase=800000000      cpu=59166.90



Finished simulation

Total cpu time for this run:            0.00 (sec.) 0.0000(hours)
CPU time including previous runs:       59166.90 (sec.) 16.4352(hours)
Histories per hour:                     4.86759e+07
Number of random numbers used:          567595259046
Number of electron CH steps:            3.135e+10
Number of all electron steps:           4.27087e+10


last case = 800000000 fluence = 80000

Geometry                        Cavity dose
------------------------------------------------
Geometry Type: EGS_EnvelopeGeometry     CHAMBER_IP_R3              4.8453e-12 +/-
0.107  %



End of run                                                Wed Apr 12 00:09:50 2017
=============================================================================
```

A26MR ionization chamber

```
            ***********************************************
            *                                             *
            *               egs_chamber CSE)              *
            *                                             *
            ***********************************************

This is EGS_ChamberApplication Revision: 1.15  based on
EGS_AdvancedApplication Revision: 1.39



======================== geometry ====================
type = EGS_EnvelopeGeometry
name = CHAMBER_IP_R3
number of regions = 434
base geometry = phantom (type EGS_XYZGeometry)
inscribed geometries:
   CHAMBER_0_R3 (type EGS_EnvelopeGeometry)
======================================================


The simulation uses the following source:
=========================================
 Collimated source from a shape of type point onto a shape of type rectangle with
tabulated           histogram           spectrum           defined           in
/usr/local/sw/modules/source/EGSnrc/HEN_HOUSE/spectra/mohan6.spectrum, photons


Random number generator:
========================================
type                = ranmar
high resolution     = no
initial seeds       = 33 97
numbers used so far = 111842705408




The following media are defined:
================================

0  AIR521ICRU              AE= 0.5210 AP= 0.0100 0
1  C552521ICRU             AE= 0.5210 AP= 0.0100 1
2  H2O521ICRU              AE= 0.5210 AP= 0.0100 2
3  CU521ICRU               AE= 0.5210 AP= 0.0100 3
4  TEFLON521ICRU           AE= 0.5210 AP= 0.0100 4
5  POLYCARBONATE521ICRU    AE= 0.5210 AP= 0.0100 5


Transport parameter and cross section options:
==============================================
Photon cross sections                          xcom
Compton cross sections                         default
Global Pcut                                    0.01
Pair cross sections                            BH
```

```
Pair angular sampling                                Simple
Triplet production                                   Off
Bound Compton scattering                             norej
Radiative Compton corrections                        Off
Rayleigh scattering                                  Off
Atomic relaxations                                   On
Photoelectron angular sampling                       On
Photonuclear attenuation                             Off
Photonuclear cross sections                          default

Global Ecut                                          0.521
Brems cross sections                                 BH
Brems angular sampling                               KM
Spin effects                                         Off
Electron Impact Ionization                           Off
Global Smax                                          1e+10
ESTEPE                                               0.1
Ximax                                                0.1
Boundary crossing algorithm                          Exact
Skin depth for BCA                                   3
Electron-step algorithm                              EGSnrc
================================================

Variance reduction
=====================================================
Photon splitting = off
Range rejection = Russian Roullette (RR)
rejection in cavity for E < 0.521
else RR with survival probability 0.015625
rejection geometry is CHAMBER_IP_R3


photon cross-section enhancement = On
 1) CHAMBER_IP_R3
    regions    :  1 2 3 4 5 6 7 8 9 10 11 12 13 14 15 16 17 18 19 20 21 22 23 24
25 26 27 28 29 30 31 32 33 34 35 36 37 38 39 40 41 42 43 44 45 46 47 48 49 50 51
52 53 54 55 56 57 58 59 60 61 62 63 64 65 66 67 68 69 70 71 72 73 74 75 76 77 78
79 80 81 82 83 84 85 86 87 88 89 90 91 92 93 94 95 96 97 98 99 100 101 102 103 104
105 106 107 108 109 110 111 112 113 114 115 116 117 118 119 120 121 122 123 124
125 126 127 128 129 130 131 132 133 134 135 136 137 138 139 140 141 142 143 144
145 146 147 148 149 150 151 152 153 154 155 156 157 158 159 160 161 162 163 164
165 166 167 168 169 170 171 172 173 174 175 176 177 178 179 180 181 182 183 184
185 186 187 188 189 190 191 192 193 194 195 196 197 198 199 200 201 202 203 204
205 206 207 208 209 210 211 212 213 214 215 216 217 218 219 220 221 222 223 224
225 226 227 228 229 230 231 232 233 234 235 236 237 238 239 240 241 242 243 244
245 246 247 248 249 250 251 252 253 254 255 256 257 258 259 260 261 262 263 264
265 266 267 268 269 270 271 272 273 274 275 276 277 278 279 280 281 282 283 284
285 286 287 288 289 290 291 292 293 294 295 296 297 298 299 300 301 302 303 304
305 306 307 308 309 310 311 312 313 314 315 316 317 318 319 320 321 322 323 324
325 326 327 328 329 330 331 332 333 334 335 336 337 338 339 340 341 342 343 344
345 346 347 348 349 350 351 352 353 354 355 356 357 358 359 360 361 362 363 364
365 366 367 368 369 370 371 372 373 374 375 376 377 378 379 380 381 382 383 384
385 386 387 388 389 390 391 392 393 394 395 396 397 398 399 400 401 402 403 404
405 406 407 408 409 410 411 412 413 414 415 416 417 418 419 420 421 422 423 424
425 426 427 428 429 430 431 432 433
    enhancement:  64 64 64 64 64 64 64 64 64 64 64 64 64 64 64 64 64 64 64 64 64
64 64 64 64 64 64 64 64 64 64 64 64 64 64 64 64 64 64 64 64 64 64 64 64 64 64 64
64 64 64 64 64 64 64 64 64 64 64 64 64 64 64 64 64 64 64 64 64 64 64 64 64 64 64
```

```
64 64 64 64 64 64 64 64 64 64 64 64 64 64 64 64 64 64 64 64 64 64 64 64 64
64 64 64 64 64 64 64 64 64 64 64 64 64 64 64 64 64 64 64 64 64 64 64 64 64
64 64 64 64 64 64 64 64 64 64 64 64 64 64 64 64 64 64 64 64 64 64 64 64 64
64 64 64 64 64 64 64 64 64 64 64 64 64 64 64 64 64 64 64 64 64 64 64 64 64
64 64 64 64 64 64 64 64 64 64 64 64 64 64 64 64 64 64 64 64 64 64 64 64 64
64 64 64 64 64 64 64 64 64 64 64 64 64 64 64 64 64 64 64 64 64 64 64 64 64
64 64 64 64 64 64 64 64 64 64 64 64 64 64 64 64 64 64 64 64 64 64 64 64 64
64 64 64 64 64 64 64 64 64 64 64 64 64 64 64 64 64 64 64 64 64 64 64 64 64
64 64 64 64 64 64 64 64 64 64 64 64 64 64 64 64 64 64 64 64 64 64 64 64 64
64 64 64 64 64 64 64 64 64 64 64 64 64 64 64 64 64 64 64 64 64 64 64 64 64
64 64 64 64 64 64 64 64 64 64 64 64 64 64 64 64 64 64 64 64 64 64 64 64 64
64 64 64 64 64 64 64 64 64 64 64 64 64 64 64 64 64 64 64 64 64 64 64 64 64
64 64 64 64 64 64


region by region ECUT = Off

==========================================

Suming the following .egsdat files:
================================================================================
 1 ze05a26_w1.egsdat              ncase=160000000      cpu=17346.30
 2 ze05a26_w2.egsdat              ncase=160000000      cpu=16875.60
 3 ze05a26_w3.egsdat              ncase=160000000      cpu=16785.10
 4 ze05a26_w4.egsdat              ncase=160000000      cpu=17078.90
 5 ze05a26_w5.egsdat              ncase=160000000      cpu=17226.00
================================================================================
                            Total ncase=800000000      cpu=85311.90



Finished simulation

Total cpu time for this run:            0.00 (sec.) 0.0000(hours)
CPU time including previous runs:       85311.90 (sec.) 23.6977(hours)
Histories per hour:                     3.37585e+07
Number of random numbers used:          559293892148
Number of electron CH steps:            3.12946e+10
Number of all electron steps:           4.26209e+10


last case = 800000000 fluence = 80000

Geometry                         Cavity dose
------------------------------------------------
Geometry Type: EGS_EnvelopeGeometry     CHAMBER_IP_R3              4.0535e-12 +/-
0.173  %



End of run                                              Thu May 11 01:40:46 2017
================================================================================
```